

High-resolution bio- and chemostratigraphy of an expanded record of Oceanic Anoxic Event 2 (Late Cenomanian–Early Turonian) at Clot Chevalier, near Barrême, SE France (Vocontian Basin, SE France)

Andrew S. Gale¹, Hugh C. Jenkyns², Harilaos Tsikos³, Y. van Breugel⁴, Jaap S. Sinninghe Damsté^{4,5}, Cinzia Bottini⁶, Elisabetta Erba⁶, Fabio Russo⁶, Francesca Falzoni⁶, Maria Rose Petrizzo⁶, Alexander J. Dickson⁷, David S. Wray⁸

Authors' addresses:

1. School of Earth and Environmental Sciences, University of Portsmouth, Burnaby Building, Burnaby Road, Portsmouth PO1 3QL UK, E-mail: andy.gale@port.ac.uk
2. Department of Earth Sciences, University of Oxford, South Parks Road, Oxford OX1 3AN, UK
3. Department of Geology, Rhodes University, Grahamstown 6140, South Africa
4. Royal Netherlands Institute for Sea Research, Department of Marine Microbiology and Biogeochemistry, and Utrecht University, P.O. Box 59 1790 AB Den Burg (Texel), The Netherlands
5. Faculty of Geosciences, Department of Earth Sciences Utrecht University, P.O. Box 80.021, 3508 TA Utrecht, The Netherlands
6. Dipartimento di Scienze della Terra "A. Desio", Università degli Studi di Milano, via Mangiagalli 34, 20133 Milano, Italy
7. Department of Earth Sciences, Royal Holloway University of London, Egham, TW20 0EX, UK
8. School of Science, University of Greenwich, Medway Campus, Chatham, ME4 4TB, UK

Keywords. Cenomanian–Turonian boundary, biostratigraphy, geochemistry, Vocontian Basin, Oceanic Anoxic Event 2

Abstract

A newly located exposure of the Niveau Thomel, an organic-rich level at the Cenomanian–Turonian boundary, provides a highly expanded record of Oceanic Anoxic Event (OAE) 2, excepted for the lower relatively condensed glauconite-rich part of the section. The new locality, close to Barrême in the Vocontian Basin, SE France, is developed in deep-water hemi-pelagic facies (shales, marls, marly limestones, variably enriched in organic matter) and provides an improved understanding of palaeoceanographic events associated with OAE 2. Investigation of the biostratigraphy (nannofossils and planktonic foraminifera), organic and inorganic geochemistry (bulk carbonate $\delta^{18}\text{O}$, total organic carbon (TOC), bulk organic, biomarker-specific and carbonate $\delta^{13}\text{C}$, major and trace elements, and Rock-Eval data) has allowed characterization of the sediments in great detail. The combined study further constrains the detailed relationship between bio- and chemostratigraphy (particularly with respect to the details of the well-displayed positive carbon-isotope excursion) for this interval. The section also provides new evidence, in the form of a positive oxygen-isotope excursion and an offset between carbonate and organic-carbon carbon-isotope records, which confirms the importance of cooling accompanied by a drop in dissolved CO_2 in near-surface waters during the Plenus Cold Event that characterized the early part of OAE 2. Evidence for increased oxygenation of bottom waters, together with elevated concentrations of redox-sensitive and chalcophilic elements registered elsewhere through the level of the Plenus Cold Event, may be reflected in enhanced concentrations of iron (in glauconite) and nickel in coeval strata from the Clot Chevalier section.

1. Introduction

Oceanic Anoxic Event 2, which straddles the Cenomanian–Turonian Boundary (94–93 Ma), is the most striking palaeoclimatic and palaeoceanographic event of the Late Mesozoic (e.g. Arthur et al., 1988; Jenkyns 2003, 2010; Voigt et al. 2006; Gradstein et al., 2012; Jarvis et al. 2011; Meyers et al., 2012a; Batenburg et al., 2016). The event

coincides with a peak of Cretaceous greenhouse warming (e.g. Friedrich et al., 2012; O'Brien et al., 2017), and is marked globally by a major positive excursion in $\delta^{13}\text{C}$ in marine and terrestrial archives, coeval with extensive deposition in all ocean basins of planktonic organic material, caused by globally significant high productivity and local anoxic to euxinic conditions. Although the event itself was punctuated, during the latest Cenomanian, by a transient cooling episode known as the Plenus Cold Event (Gale and Christensen, 1996; Forster et al., 2007; Sinninghe Damsté et al., 2010; van Helmond et al., 2013; Jenkyns et al., 2017), palaeotemperature proxies suggest that global temperatures rose again in the early Turonian, before a reversal of the overall climatic trend and the onset of Late Cretaceous cooling (Jenkyns et al. 1994; Clarke and Jenkyns, 1999; Jarvis et al., 2011; Friedrich et al., 2012; Linnert et al., 2014; Falzoni et al., 2016a; O'Brien et al., 2017).

Based on osmium-isotope profiles from a number of sections that record an abrupt movement of global seawater to more unradiogenic values preceding the rise in $\delta^{13}\text{C}$, the initiation of OAE 2 has been attributed to a major pulse in some kind of basalt–seawater interaction such as mafic magmatic/volcanic/hydrothermal activity (Turgeon and Creaser 2009; Du Vivier et al., 2014, 2015; Jenkyns et al., 2017), which raised $p\text{CO}_2$ and stimulated oceanic productivity through direct input of trace elements, as well as by an accelerated hydrological cycle fostering increased fluvial input of nutrients to the oceans (e.g. Sinton and Duncan, 1997; Jones and Jenkyns, 2001; Jenkyns, 2003; Snow et al., 2005). Neodymium-isotope records from sections in the proto-Atlantic and European areas suggest reorganizations of oceanic circulation and bottom-current activity during this interval of major environmental change (Martin et al., 2012; Zheng et al., 2013, 2016). However, the nature and timing of feedback mechanisms, particularly as regards the relative roles of organic-carbon burial and mafic/felsic silicate weathering in drawing down CO_2 , remain uncertain (Blättler et al., 2011; Jarvis et al., 2011; Pogge von Strandmann et al., 2013). Hence, improved understanding of the causes and effects of OAE 2 is dependent upon the discovery of stratigraphically expanded, complete successions.

The Vocontian Basin in south-east France is situated on the northern margin of Tethys, set between the Subalpine Chain and the Provence Platform (Fig. 1A–C). The central region of the basin contains an expanded hemipelagic succession of

Lower Cretaceous and Cenomanian shales, marls and marly limestones, which pass laterally into sandy marls towards the basin margins (Crumière 1989; Crumière et al. 1990). The hemipelagic sediments are overlain by pelagic limestones of Turonian to Campanian age. The uppermost Cenomanian in the central basin is represented by a dark organic-rich calcareous shale/marl, called the *Niveau Thomel* (Thomel Level) by Crumière (1989), after Gérard Thomel, who studied Cenomanian ammonites from this region. This interval has been the subject of several biostratigraphic and geochemical studies, based primarily on the sections at Vergons and Ondres (Fig. 1A; Crumière 1989; Crumière et al. 1990; Grosheny et al. 2006;), Pont d'Issole (Morel 1998; Grosheny et al. 2006; Jarvis et al. 2011), Les Lattes (Grosheny et al. 2017) and Lambruisse (Takashima et al. 2009; Fernando et al., 2010). These studies have demonstrated the presence in the Vocontian Basin of an expanded representation of OAE 2 that displays a complete, ornate, positive excursion in $\delta^{13}\text{C}$ in bulk carbonate and bulk organic matter, associated with two discrete organic-rich levels, Th1 and Th3. These records have been calibrated biostratigraphically by the use of planktonic foraminifera, nannofossils and dinoflagellates, and provide an important and instructive record of OAE 2 in a deep-water setting on the northern continental margin of the Tethys Ocean (Jarvis et al. 2011).

In this paper, the stratigraphy and geochemistry of an exceptionally expanded exposure of the Thomel Level at Clot Chevalier, north of the village of St. Lions, near Barrême in Haut Provence is described (Figs 2, 3, 4). Using high-resolution sampling (every 30 cm), $\delta^{13}\text{C}_{\text{org}}$, $\delta^{13}\text{C}_{\text{carb}}$ and $\delta^{18}\text{O}_{\text{carb}}$ curves have been generated, accompanied by compound-specific isotope data, TOC and Rock-Eval determinations and a trace-element record, calibrated against planktonic foraminiferal (Falzoni et al. 2016b) and nannofossil biostratigraphy. These data provide new insights into the precise relationship between carbon isotopes, trace elements and organic-carbon flux during the interval of major environmental change represented by OAE 2.

2. Geological setting and lithological succession

The locality is situated approximately 200 m north-east (upstream) of the classical St Lions locality of Gérard Thomel (Figs 2, 3), which exposes middle Cenomanian

hemipelagic chalks, and is famous for the ammonites found in a hard limestone bed (Gale 1995). The Clot Chevalier locality, which exposes the Niveau Thomel (Fig. 4), was discovered accidentally by the lead author (ASG) in 2003.

The lithostratigraphic nomenclature used here (Fig. 3) follows Jarvis et al. (2011), who subdivided the Thomel Level into four units (Th1–4). At Clot Chevalier, the basal 3 m of succession comprise thinly bedded alternations of bioturbated marly limestones and marls with low TOC values (< 0.2%). The base of the Thomel Level (~2.5 m above the zero datum level henceforth taken as the base of the section; Fig. 5) is a sharply defined surface, perforated by obliquely oriented, dark-filled *Planolites* burrows that descend for 0.3 m beneath the surface. Unit Th1 is a glauconitic mid-grey marl, 1.05 m in thickness, but not conspicuously darker than the underlying sediments; it contains 1.5–2.0% TOC. Unit Th2 (2.1 m), also glauconitic, consists of five thin marly limestones that alternate with bioturbated marls, with overall TOC values generally lower than those of Th1. Unit Th3 (17.8 m) comprises dark grey sub-laminated marls containing two levels of more calcareous, non-laminated beds (9.5–10.3 m; 13.3–14.8 m). TOC levels are tolerably high throughout, but fluctuate between 0.5 to 1.5% in about 10 well-defined peaks and troughs. The base of Unit Th4 is taken arbitrarily above a thick (1.5 m) bed of marly limestone, which contains a thin sharply defined siliciclastic bed, probably a turbidite (0.1 m), at a level ~ 23.7m above the base of the section). The upper surface of Th4 cannot be accurately defined. There are two bedding-parallel fracture surfaces marked by calcite veins within Th3, but otherwise there is no evidence of any tectonic displacement or re-deposition, other than the presence of the two thin clastic turbidites (fine sand), indicated in Fig. 4. The section has not yielded any ammonites or other diagnostic macrofossils, and they are also absent from black shales of comparable age in the Vocontian Basin.

2.1 Comparison with other sections in the Vocontian Basin

Correlation with other sections in the Vocontian Basin is shown in Fig. 3B. Ondres (1), Pont d'Issole (2), Lambruisse (3), and Clot Chevalier (4) fall on an approximately NE–SW transect, and demonstrate a progressive southwesterly expansion of the

Niveau Thomel. The Vergons section (5), to the ESE of Clot Chevalier, also displays an attenuated succession, and lies close to the southern margin of the basin.

At Lambruisse (Crumière 1989; Takashima et al. 2009) and Pont d'Issole (Jarvis et al. 2011), the base of the Thomel Level is represented by a gradational lithological transition from the underlying marly chalks, whereas at Ondres and Vergons the base is sharp and was identified as a minor hiatus by Crumière (1989) and Crumière et al. (1990). At Clot Chevalier, the base is conspicuously burrowed, and the lower relatively organic-rich Unit Th1 (lower black shales of Jarvis et al. 2011) is thin (1 m), as compared with 6 m at Pont d'Issole (Jarvis et al. 2011), 3 m at Lambruisse (Takashima et al. 2009) and approximately 2 m at Vergons and Ondres (Fig. 3B) (Crumière et al. 1990). Unit Th2 is of more even thickness across the basin (2 m, Clot Chevalier; 3 m Pont d'Issole; 4 m, Lambruisse) and always consists of thinly bedded marls and marly limestones with relatively low total organic carbon (TOC) values, with maxima of 2%. Unit Th3 (upper black shales of Jarvis et al. 2011) is considerably thicker at Clot Chevalier and, at 17 m from base to top, represents the most expanded development known in the Vocontian Basin (9 m Lambruisse; 6.3 m Pont d'Issole). This degree of stratigraphic expansion is significant because Th3 contains most of the positive carbon-isotope excursion of OAE 2.

In summary, the Clot Chevalier Thomel Level section is characterized by:

- 1) a minor hiatus at the base of Th1,
- 2) a relatively thin glauconitic representation of Th1,
- 3) a somewhat condensed glauconitic but regionally typical development of Th2,
- 4) a relatively expanded representation of Th3.

The presence of a sharp break at the base of the succession has been noted widely, from the Anglo-Paris Basin (sub-plenus erosion surface; Jefferies 1962, 1963), Germany (Fazieswechsel: Voigt et al. 2008) across to the Crimea (Gale et al. 1999) and is clearly a regional phenomenon recording erosion and/or non-deposition and/or dissolution. The presence of glauconite in Th1 and Th2 is symptomatic of slow net rates of sedimentation and/or erosion (Cloud, 1955; Odin and Matter, 1981).

3. Calcareous nannofossil biostratigraphy

3.1. Materials and methods

A total of 37 samples throughout the section were analyzed for biostratigraphy. Semi-quantitative analyses of calcareous nannofossils (Table 1) were performed on smear slides using standard light microscope techniques under cross-polarized and transmitted light, at $\times 1250$ magnification. Smear slides were prepared following the methodology described by Monechi & Thierstein (1985). A small amount of rock material was powdered into an agate mortar with few drops of bi-distilled water and placed onto a glass coverslip. Using a toothpick, the suspension was repeatedly smeared along the coverslip until the required thickness of smear was achieved and dried on a hotplate. The coverslip was mounted to the glass slide with Norland Optical Adhesive, and glued by exposure to UV light for a few minutes.

The taxonomic concepts for calcareous nannofossil species identification (Taxonomic Appendix) follow the original descriptions and the discussions by Perch-Nielsen (1985), Burnett (1998) and Lees (2007). At least two traverses of each smear slide were studied. Calcareous nannofossils were typified for preservation and total abundance as described below. Total abundance: H = high (more than 51% of all particles); M = moderate (11%–50% of all particles); L = low (1%–10% of all particles); VL = very low (less than 1% of all particles). Single taxon abundance: A = abundant (more than 11 specimens per field of view); C = common (1–10 specimens per field of view); F = few to frequent (1 specimen per 2–20 fields of view); R = rare (1 specimen per more than 20 fields of view)

Preservation: VG = very good preservation (no evidence of dissolution and/or overgrowth, no alteration of primary morphological characteristics. All specimens are identifiable to the species level); G = good preservation (little or no evidence of dissolution and/or overgrowth, primary morphological characteristics only slightly altered, most specimens are identifiable to the species level); M = moderate preservation (some evidence of dissolution and/or overgrowth, primary morphological characteristics somewhat altered, most specimens are identifiable to the species level); P = poor preservation (overgrowth and/or dissolution is extensive, making identification of some specimens difficult); VP = very poor preservation (severely etched and/or overgrown, primary morphological characteristics largely

destroyed, fragmentation has occurred, and specimens are often unidentifiable at the species and/or generic level).

3.2 Results

Nannofossil preservation is generally poor-moderate to moderate throughout the section and total abundance varies from low-medium to medium-high. Abundance and occurrence of identified taxa are reported in the range chart (Table 1). A total of 115 taxa have been observed, and the most common and/or important species for biozonation in the studied section are illustrated in Figure 6.

The adopted calcareous nannofossil biozonations follow Sissingh (1977) as implemented by Perch-Nielsen (1985), Bralower et al. (1995), Burnett (1998) and revised by Gambacorta et al. (2015). Nannofossil zonal and subzonal markers identified are listed in Table 2 together with planktonic foraminiferal markers (Falzoni et al., 2016b). Based on bioevents, zones and subzones were determined (Fig. 5). Following Burnett (1998), zones and subzones UC3d–UC7 were identified. All the zonal and subzonal markers were recognized but manifested themselves in a different sequence of events. Specifically, the HO (highest occurrence) of *Cretarhabdus striatus* co-occurs with the HO of *Lithraphidites acutus*, the LO (lowest occurrence) of *Quadrum intermedium*-5 occurs above the HO of *Helenea chiastia*, and *Eprolithus moratus* has its LO in the same sample as that recording the LO of *Quadrum gartneri*. This stratigraphic pattern of datum levels prevented the subdivision of the section into subzones UC4a/UC4b, UC5b/UC5c and UC6a/UC6b.

Following Bralower et al. (1995) and Gambacorta et al. (2015), all the zonal and subzonal markers were recognized and zones NC11* - NC13** were identified. All zonal and subzonal markers of the Sissingh's zonation (1977) were detected allowing the identification of zones CC10 - CC11.

Based on semiquantitative abundances, nannofossil assemblages characterize specific intervals, from oldest to youngest (Fig. 5; Table 1).

Interval A (0 to 6.3 m) corresponds to the *R. cushmani* Zone and lowermost part of the *W. archaeocretacea* Zone, the lithological units Th1 and Th2 and to the interval characterized by the rise of $\delta^{13}\text{C}$ values to peak 'a'. The assemblage comprises common *Watznaueria barnesia*, representing the dominant taxon, and

frequent to common *Biscutum constans*, *Eiffellithus turriseiffelii*, *Rhagodiscus achlyostaurion* and *Watznaueria manivitiae*. Other frequent taxa are *Eprolithus floralis*, *Helicolithus trabeculatus*, *Prediscosphaera cretacea*, *Prediscosphaera ponticula*, *Retecapsa angustiforata*, *Retecapsa crenulata*, *Tranolithus orionatus*, *Zeugrhabdotus diplogrammus*, *Zeugrhabdotus embergeri*, *Zeugrhabdotus howei* and *Zeugrhabdotus noeliae*.

Interval B (6.3 to 20.25 m) corresponds to the lower and middle part of the *W. archaeocretacea* Zone, most of the lithological unit Th3 and the interval between peaks 'b' and 'c' of the $\delta^{13}\text{C}$ anomaly. The assemblage is similar to that of Interval A, but shows a decrease in the abundance of *Broinsonia signata*, *Calcioselenia fossilis*, *Calculites percensis*, *Gartnerago segmentatum*, *Sollasites horticus* and *Tranolithus minimus*. In this interval, *Tranolithus gabalus* and *Zeugrhabdotus erectus* (large form) are present in a more continuous way.

Interval C (20.25 to 34.8 m) coincides with the upper part of the *W. archaeocretacea* Zone, the uppermost part of lithological unit Th3 through Th4, and the recovery of the $\delta^{13}\text{C}$ curve. The assemblage is still dominated by the same taxa of Intervals A and B, although there is an increase in the relative abundance of *Amphizygus brooksii*, *Eiffellithus gorkae*, *Eiffellithus perchnielseniae*, *Helicolithus trabeculatus*, *Microrhabdulus decoratus*, *S. horticus* and *T. orionatus*.

Remarkably, nannofossil assemblages A to C correlate with intervals marked by different species (and to a lower extent genera) richness. Minimum diversity is observed in the middle part of the 'b' to 'c' isotopic plateau (nannofossil zones UC5 and lower part of UC6).

4. Geochemistry

4.1 Material and methods

All 118 samples collected were analyzed for bulk major and trace elements, calcium carbonate, total organic-carbon (TOC), and bulk-carbonate carbon-isotope ratios (data illustrated in Falzoni et al. 2016b), whereas 36 samples with TOC contents higher than 0.7 wt% were also analyzed for bulk organic carbon-isotope values a subset of which was analyzed for biomarkers.

Quantification of major-, trace- and rare-earth element abundance was undertaken at the University of Greenwich by first grinding samples to a fine powder in an agate ball mill, drying at 105°C and dissolving *via* a lithium metaborate fusion procedure (see Wray and Wood 1998). Analysis of the prepared solution was undertaken using a combination of a Thermo iCAP 6500 ICP-OES and a Thermo Elemental X2 ICP-MS with instrumentation calibrated using traceable, matrix-matched, synthetic calibration standards supplied by an ISO Guide 34 accredited supplier. The testing laboratory holds United Kingdom Accreditation Service (UKAS) accreditation to ISO17025 for this method. Validation of the method was achieved using a range of geological reference materials. An in-house QC sample was included with each tray of fusions and the data from these QC samples were evaluated via a Shewhart chart as part of our standard operating procedure. Five lithium metaborate blanks were also included in the unit of work and all presented data have been blank subtracted. Six geological reference materials (CRPG ACE, BEN & GSN, USGS MAG & SCo-1 and NIST NBS 1c) were also prepared and analyzed at the same time as the samples forming this study and their data evaluated. Uncertainty of measurement was within 3% (relative) for all major elements and within 10% (relative) for all trace elements.

Samples of fine-grained limestones were analyzed for $\delta^{13}\text{C}$ and $\delta^{18}\text{O}$ using a VG Isogas Prism II mass spectrometer with an on-line VG Isocarb common acid bath preparation system at the Department of Earth Sciences at Oxford University. Samples were doused with acetone ($(\text{CH}_3)_2\text{CO}$) and dried at 60°C for at least 30 minutes. In the instrument they were reacted with purified phosphoric acid (H_3PO_4) at 90°C. Calibration to the VPDB standard via NBS-19 was made daily using the in-house (NOCZ) Carrara marble standard. Reproducibility of replicated standards is usually better than 0.1‰ for $\delta^{13}\text{C}$ and $\delta^{18}\text{O}$. Stable-isotope ratios are reported using the conventional δ notation to indicate per mil (‰) deviation from the VPDB standard. Bulk organic-carbon isotope values were derived from de-carbonated samples, obtained by treatment with dilute HCl at ambient temperature, which were analyzed at the Research Laboratory for Archaeology at Oxford University using a Carlo-Erba elemental analyzer connected to a PDZ Europa Geo-20-20 stable isotope-ratio mass spectrometer. The measurements were standardized using Nylon 66

($\delta^{13}\text{C}_{\text{nylon}} = -26.16 \pm 0.21\text{‰}$) and expressed as per mil (‰) deviation from the Vienna Pee Dee Belemnite (VPDB) standard. All results are accurate to better than $\pm 0.2\text{‰}$.

Values of TOC in wt% were determined on all samples using a Strohlein Coulomat 702 as described by Jenkyns (1988) and Kolonic et al. (2002). For the biomarker analyses, a total of 17 out of the 36 organic-rich samples were sub-selected based on a combination of bulk TOC content and stratigraphic position, in order to provide a sufficiently well-resolved stratigraphic view of compound-specific isotopic data and their variations. Between 14 and 35 g of bulk-rock powders for the selected samples were solvent-extracted with a mixture of dichloromethane (DCM) and methanol (MeOH) (9:1, v/v) using accelerated solvent extraction (Dionex ASE 200) in three cycles under conditions of 100°C and 1000 Psi (5 min static, 100% flush, 90s purge) at NIOZ. Total Lipid Extracts (TLE) were stripped off dissolved elemental sulfur using a small column of activated copper, and subsequent yields ranged between 7 and 26 mg. The TLE's were separated by standard Al_2O_3 column chromatography into an apolar fraction (eluent hexane/DCM, 9:1, v/v), a pure DCM-fraction, a tetraether fraction (eluent DCM/MeOH, 95:5, v/v) and a polar fraction (eluent MeOH/DCM, 1:1, v/v). The total apolar fraction was first analyzed by gas chromatography (GC-FID coupled with FPD, enabling the detection of sulfur-containing compounds) and then by gas chromatography-mass spectrometry (GC-MSD). The saturated and unsaturated compounds in the apolar hydrocarbon fraction were separated using a AgNO_3 -impregnated silica column eluted with hexane and ethyl-acetate, respectively.

Compound-specific $\delta^{13}\text{C}$ analyses were performed for the aliphatic saturated and unsaturated hydrocarbon fractions and the apolar fraction of the desulfurized polar fractions where possible. The isotope-ratio-monitoring GC-MS (irmGCMS) system used is, in principle, similar to the DELTA-S system described by Hayes et al. (1990). The instrument specifications, column conditions and temperature program were the same as described above for GC analyses. The $\delta^{13}\text{C}$ values for individual compounds are reported in the standard delta notation against VPDB standard, and duplicate runs yield a precision of ± 0.1 to 1.4‰ (average 0.5‰). An internal standard was added to the TLEs for the quantification of apolar hydrocarbon compounds.

Rock Eval data were generated on a Rock Eval 6 instrument with a 'standard' configuration located at the University of Greenwich. Instrument calibration was achieved using the IFP160000 standard and verified using Norwegian Petroleum Directorate reference materials SR-1 and JR-1, and an in-house QC sample was included at regular intervals through the analytical sequence. All samples were tested but only those with a total organic carbon (TOC) content >0.5% are presented here since Rock Eval data from sediments with a TOC value <0.5% are not deemed to be as reliable (Behar et al., 2001).

4.2. Results

4.2.1 Chemostratigraphy

The bulk of the TOC determinations fall in the range of 0.5 to 1.5%, overlapping with those reported from the Vergons and Pont d'Issole sections without, however, any values in excess of 2% (cf. Crumière et al., 1990; Jarvis et al., 2011). As is the case with most sections that record OAE 2, the most TOC-rich intervals are generally the least rich in calcium carbonate (Fig. 7). The stratigraphically irregular TOC profile persists if the data are recalculated on a carbonate-free basis, implying that the cyclic pattern of organic-matter enrichment is a primary sedimentary feature, probably responding to climatically forced changes in productivity of near-surface waters and/or enhanced burial efficiency due to better preservation. These shifts in carbonate:TOC ratio through the section could hence have been caused by changes in the chemical composition of the dominant planktonic biota - radiolarians are most abundant in the organic-rich facies (Falzoni et al., 2016b) - or fluctuating ambient pH conditions resulting in sea-floor dissolution of carbonate (e.g. Jenkyns, 2010). Similar patterns of alternating organic-rich and carbonate-rich pelagic facies through the OAE 2 interval are recorded in deep-water limestones in Sicily, and from northern Germany in stratigraphic equivalents to the English Chalk, and have been attributed to a dominant 100-ky orbital-climatic control (Scopelliti et al., 2004; Voigt et al., 2008). However, detailed analysis of OAE 2 sections from proto-Nrth Atlantic sites has underscored the role of obliquity as a prime control on sedimentary cyclicity (Meyers et al., 2012b). Given its palaeolatitude, similar forcing functions may have operated in the Vocontian Basin, as exemplified by the Clot Chevalier section.

Carbon-isotope data for bulk carbonate and TOC across the examined stratigraphic profile (Fig. 7) record the characteristic positive isotopic excursion that typifies this global event, conventionally attributed to globally increased sequestration of marine organic matter relatively enriched in the lighter isotope ^{12}C (e.g. Scholle and Arthur, 1980; Arthur et al., 1987; Schlanger et al., 1987; Tsikos et al., 2004; Figs 5, 7 herein). Pre-excursion values for $\delta^{13}\text{C}_{\text{carb}}$ are essentially invariant at $\sim 2.6\text{‰}$ over the stratigraphically lowermost 2 m of section. A sharp rise in $\delta^{13}\text{C}_{\text{carb}}$ is seen thereafter in a step-wise fashion: first to a narrow plateau of 1.8 m stratigraphic extent at an average $\delta^{13}\text{C}_{\text{carb}}$ value of $\sim 3.5\text{‰}$, followed by a second rise to 4.1‰ at $\sim 5.4\text{m}$ above the base of section (peak 'a'). The $\delta^{13}\text{C}_{\text{carb}}$ values then decline sharply to $\sim 3.1\text{‰}$ and then rise again to $\sim 4.1\text{‰}$ over 1.2 m of section, defining the most noteworthy negative excursion. From that point upwards, the well-documented plateau interval of maximum $\delta^{13}\text{C}_{\text{carb}}$ values, as typically seen in OAE 2 sections elsewhere, develops over a stratigraphic thickness of approximately 13.2 m. Over this interval, from peak 'b' to peak 'c', the $\delta^{13}\text{C}_{\text{carb}}$ data fluctuate about an average $\delta^{13}\text{C}_{\text{carb}}$ value of $\sim 4\text{‰}$, although there is a noteworthy drop in values of $\sim 0.5\text{‰}$ over the 13–15 m interval. The highest point of the isotopic plateau is recorded at $\sim 20\text{ m}$ above the base of section, and is in fact the highest $\delta^{13}\text{C}_{\text{carb}}$ value of the entire dataset obtained here (4.4‰) and lies close to the Cenomanian–Turonian boundary (Falzoni et al., 2016b). Up-section, $\delta^{13}\text{C}_{\text{carb}}$ values progressively decline to $\sim 2.8\text{‰}$ at $\sim 27\text{ m}$ above the base of section, i.e. over a stratigraphic distance of 7.5 m, before they become practically invariant over the remaining 7.5 m of the sampled section, continuing above the Thomel Level, with an average value of $\sim 3.2\text{‰}$.

The bulk organic-carbon (TOC) isotope curve records a smoother profile across the stratigraphy, in part due to the lower resolution: $\delta^{13}\text{C}_{\text{TOC}}$ values rise sharply from a minimum of -25.8‰ at $\sim 2.4\text{ m}$ above the base of section, to a maximum value of -23.5‰ some 4.2 m higher. The latter value is also the maximum $\delta^{13}\text{C}_{\text{TOC}}$ value of the entire dataset obtained in this study. $\delta^{13}\text{C}_{\text{TOC}}$ values then decline rather sharply to -24.3‰ over a narrow stratigraphic interval of $\sim 1.5\text{ m}$, and remain at an average of -24.1‰ over another 11.7 m of section but also defining a drop (in this case of $\sim 0.2\text{‰}$) over the 13–15m interval. From $\sim 20\text{ m}$ until $\sim 29\text{ m}$ above the

base of section, the $\delta^{13}\text{C}_{\text{TOC}}$ record shows an overall decline of approximately 1‰, i.e. it drops to a value of -24.9‰ just below the top of the Thomel Level.

Over the stratigraphic interval recording the isotopic plateau for both $\delta^{13}\text{C}_{\text{carb}}$ and $\delta^{13}\text{C}_{\text{TOC}}$, i.e. between 6.6 and 22.2 m above the base of section between peaks 'b' and 'c', the corresponding TOC record has an average value of ~0.9%, with a maximum of 1.67% at 12.3 m (Fig. 7). Outside that stratigraphic interval, the average TOC content is at a value of ~0.25% with very occasional spikes at around 1wt% TOC or higher.

The bulk oxygen-isotope profile shows a long-term trend of progressively lower values over the -3‰ to -4‰ range, extending from the upper Cenomanian into the Turonian, with one relatively large excursion to heavier values (maximum $\delta^{18}\text{O} = -2.6‰$) over the 4–7 m interval, which correlates with generally rather low (with one interval excepted) TOC values and dips in the carbon-isotope profile (Fig. 7). A similar excursion in $\delta^{18}\text{O}$ values is not obvious in the Pont d'Issole section (Jarvis et al., 2011).

4.2.2 Rock-Eval data

The Rock-Eval numerical data are presented in Fig. 8. The Hydrogen Index (HI) of most samples of the Thomel Level falls between 100 and 300 mg HC/gTOC. The pseudo-van Krevelen plot suggests that the organic matter is predominantly of Type II but affected by variable degrees of oxidation, with possibly an admixture of terrestrial higher plant material. A stratigraphic plot of Oxygen Index (OI) and TOC indicates that there is a gradual decrease in OI values up-section to a height of about 14 m, at which point the OI index climbs and becomes more erratic. The falling OI is interpreted as indicating the preservation of an increasing amount of marine-derived material, such as algae and cyanobacteria, deposited on the sea floor, as indicated by the organic geochemistry (see below). The erratic fluctuation in OI above 14 m is interpreted as either reflecting an increase in the contribution from terrestrial higher plant material or greater oxidation of marine organic matter prior to burial.

When compared with samples of the Thomel Level from the Vergons Section where black laminated shales are better developed (Crumi re et al. 1990; Fig. 1A,

1C) the HI values from Clot Chevalier are considerably lower, suggesting deposition in a more oxygenated environment with more degradation of marine organic matter and/or incorporation of relatively more terrestrial material. These geochemical indices are all probably linked to the overall palaeogeography of the basin, with the Clot Chevalier site formerly situated in a marginal position with the locus of major organic-matter deposition situated further to the east (Fig. 1, A, C; Crumière, 1989).

4.2.3 Inorganic geochemistry

The abundances and concentrations of major element oxides and trace elements, if normalized against the abundance of bulk aluminium oxide, show in the majority of cases, positive correlations at confidence levels that range from excellent ($R^2 > 0.9$ for K_2O , TiO_2 , Rb, Ga, Cs, Th, Be and Ta) to very good ($0.9 > R^2 > 0.8$ for SiO_2 , Fe_2O_3 , MgO, Na_2O , Sc, Hf and REE), to satisfactory ($0.8 > R^2 > 0.7$ for Zr, U, Cr and Pb). These relationships suggest a clear association of all these chemical constituents with the fine-grained terrigenous siliciclastic fraction of the studied rocks. The good correlation of iron with aluminium indicates that it is unlikely that pyrite formation was significant, unlike glauconite which was common in the lower part of the section, and stratigraphic evaluation of Fe/Al against either molybdenum enrichment factor or TOC shows very limited correlation (Fig. 9). Most of the remaining elements display either very weakly positive or statistically no relationship with the alumino-silicate fraction of the rocks whereas only Ca and Sr exhibit clear antithetic relationships to the latter and therefore confirm their expected strong geochemical association with the calcareous fraction of the samples.

Evaluation of elements considered to be redox-sensitive (U, V, Mo & Ni) was assisted by the calculation of enrichment factors (EF) using the formula:

$$EF_{element\ x} = \frac{X_{sample}/Al_{sample}}{X_{average\ shale}/Al_{average\ shale}}$$

Average shale values were taken from Wedepohl (1971, 1991) as reported in Tribouvillard et al. (2006).

Of the redox-sensitive elements examined (U, V, Mo & Ni), molybdenum displays the clearest association with TOC content (Figs 9) and also the highest

enrichment factors (EF maximum 6.8), Vanadium and uranium show evidence of enrichment correlating to local TOC maxima (V EF maximum 2.8; U EF maximum 2.1) but for much of the organic-rich interval their enrichment factors are close to 1. Nickel enrichment factors are generally less than one but again there are local high points corresponding to TOC maxima except in the interval 3–7 m, where Fe/Al ratios also reach peak values and glauconite is present. With reference to Turgeon and Brumsack (2006), Tribovillard et al. (2006, 2012) and Algeo and Tribovillard (2009), the enrichment factors for this section are seen to be relatively low (Fig. 10) when compared to those reported for organic-rich OAE 2 sections from Atlantic deep-sea drilling sites, Tarfaya, Morocco and the Bonarelli Level (TOC commonly in the range 20–25 wt% in some levels) that typically characterizes the uppermost Cenomanian in Marche–Umbria, central Italy (Farrimond et al., 1990; Tsikos et al., 2004; Erbacher et al., 2005; Jenkyns et al., 2007; Gambacorta et al., 2015; Dickson et al., 2016). The low enrichment of key redox-sensitive elements and the absence of a major iron enrichment in the Clot Chevalier section indicates that the region around the sediment-water interface during deposition of the organic-rich clays was most likely only moderately depleted in oxygen and, when the higher parts of the measured succession (above 22 m) were laid down, relatively normal oxic marine conditions existed.

4.2.4 Biomarkers

The distribution of biomarkers was studied in the extracts of the 17 selected TOC-rich sediments (Fig. 11). The *n*-alkane distribution as revealed by ion chromatograms of *m/z* 57 ranges from *n*-C₁₅ to *n*-C₃₅ and is dominated by short-chained compounds below *n*-C₁₉. The primary biological sources of *n*-alkane homologues between *n*-C₁₆ and *n*-C₁₈ are typically aquatic algae or cyanobacteria (Brassell et al., 1978; Farrimond et al., 1990), indicating a predominantly marine origin in this particular palaeoenvironmental setting. Minor amounts of *n*-alkane homologues (*n*-C₂₇ - *n*-C₃₅) do occur, and the odd-over-even carbon-number pre-dominance of *n*-alkanes indicates that they are primarily derived from terrestrial higher plants (e.g. Kuypers et al., 1999).

The isoprenoids pristane and phytane are the most prominent compounds in the total ion chromatograms (TIC) of the apolar fractions, with the former being slightly more abundant. In most marine settings, both compounds are derived mainly from chlorophyll produced by phytoplankton. Other isoprenoids do occur in the sediments but were not investigated in detail, except for lycopane that co-elutes with *n*-C₃₅ (indicative of elevated mass spectral fragments *m/z* 113, 253 and 183). The occurrence of lycopane has potential palaeoenvironmental implications suggesting oxygen-depleted conditions, at least within parts of the water column favoring the preservation of the compound, by analogy with recent oxygen minimum zones (Sinninghe Damsté et al., 2003).

Steranes form a biomarker group of eukaryotic origin (mainly algae to higher plants; review in Volkman et al., 1998). The 5 α ,14 α ,17 α (H)-20R isomers of three regular C₂₇ to C₂₉ steranes are the dominating compounds in the *m/z* 217 ion chromatogram, which shows that C₂₇ and C₂₉ steranes are more abundant than C₂₈. No 14 β ,17 β (H) - or 20S-isomers- were detected, but minor amounts of C₂₇-C₂₉ steranes with the 5 β ,14 α ,17 α (H)-20R configuration were found. These observations indicate that the organic matter is thermally immature.

The distribution of hopanoids, i.e. compounds derived from prokaryotic biological sources (bacteria and cyanobacteria, e.g., Ourisson et al., 1979; Sinninghe Damsté et al., 2003; Kuypers et al., 2004), is dominated by C₂₉ and C₃₀ neohopene, and another C₃₀-hopene, in the TIC and the *m/z* 191 ion chromatogram. Significantly, the C₂₈ neohopene, detected as an abundant biomarker in OAE 2 black shales deposited under euxinic conditions (Sinninghe Damsté et al., 2014), was not detected in these sediments. 17 β ,21 β (H)-, 17 α ,21 β (H)- and 17 β ,21 α (H)-hopanes occur as a homologous series ranging from C₃₀ to C₃₅ that is dominated by the C₃₀ and C₃₁ homologues. Consistent with a low maturity of the organic material, the 17 β ,21 β (H)-isomer shows a relatively much higher abundance. A hopanoid thiophene was identified based on the diagnostic fragments of *m/z* 97, 287, 369 and a molecular ion of 508 (30-(2'-methylenethienyl)-17 β ,21 β (H)-hopane; Valisoolalao et al., 1984). The presence of a few more sulfur-containing compounds is also indicated by the sulfur-selective FPD detector. Generally, the occurrence of such compounds suggests that sulfur incorporation into the organic matter has taken place, most

likely at an early diagenetic stage (e.g., Werne et al., 2000). In the apolar fraction of the desulfurized polar fraction, the C₃₅ 17 β ,21 β (H)-hopane was the dominant component in all sediments, together with phytane. Isorenieratane, a biomarker for the existence of photic-zone euxinia in the palaeoenvironment, was not detected in this fraction, whereas it commonly occurs in Atlantic OAE 2 black shales (Sinninghe Damsté and Köster, 1998). Overall, therefore, in terms of indicating only moderate oxygen depletion at the Clot Chevalier site during OAE 2, the biomarker data are in accord with inferences gleaned from the Rock-Eval results and inorganic geochemistry.

4.2.5 Compound-specific isotopic relationships

The profiles of Fig. 11 illustrate some of the key stratigraphic relationships between compound-specific and corresponding bulk-rock isotopic data for the selected subset of samples that was analyzed at molecular level. Complete carbon-isotope profiles are specifically presented for a series of biomarkers that are predominantly derived from marine photo-autotrophic phytoplanktonic and bacterial (including cyanobacterial) sources, namely phytane, pristane, C₃₁ hopane, C₂₇-C₂₉ steranes, whereas less complete profiles were obtainable for sulfur-bound phytane and C₃₅ hopane. As observed in previous studies (e.g. Kuypers et al., 1999, 2002, 2004; Tsikos et al., 2004; Sinninghe Damsté et al., 2008, 2010), the geometry of all compound-specific biomarker carbon-isotope profiles is rather similar to the $\delta^{13}\text{C}_{\text{TOC}}$ profile (Fig. 11), which indicates that $\delta^{13}\text{C}_{\text{TOC}}$ has not been not significantly affected by changes in OM sources, even though sulfurisation of organic matter took place in the palaeoenvironment, which can significantly influence the $\delta^{13}\text{C}_{\text{TOC}}$ (cf. Sinninghe Damsté et al., 1998). However, the maximum isotopic excursion revealed by these records varies from 2.5‰ (pristane, phytane, steranes, S-bound phytane) to 4–4.5‰ (hopanes, S-bound C₃₅ hopane). A larger isotopic excursion for hopanoids has been noted before for OAE-2 black shales of the Cape Verde basin (Sinninghe Damsté et al., 2008; C₃₁ and C₃₂ hopane, C₃₅ S-bound hopane) and the Newfoundland Basin (van Bentum et al., 2012).

5. Discussion

5.1 Stratigraphic constraints

The stratigraphically expanded section at Clot Chevalier provides insights into the detailed structure of OAE 2 in the hemipelagic deep-water setting (c. 500 m) of the Vocontian Basin, situated at a palaeolatitude of about 30°N on the northern margin of the Tethys (Jarvis et al. 2011). The upper part of the OAE 2 interval at this site is also unusually expanded. The typical structure of the carbon-isotope curve, expressed in both carbonate and organic-carbon archives, is well displayed, and patterns of TOC enrichment show a clear cyclic pattern expressed against relatively low contents of calcium carbonate, both probably reflecting changes in the nature of plankton productivity and preservation under orbital-climatic control.

The integration of calcareous nannofossil and planktonic foraminiferal biostratigraphy with the carbon-isotope record allows a high-resolution stratigraphic characterization of the Clot Chevalier section and provides further information regarding the stratigraphic distribution of nannofossils and planktonic foraminifera with respect to OAE 2 and the Cenomanian–Turonian boundary. The planktonic foraminifera dataset indicates that the extinction of *R. cushmani* at Clot Chevalier is below peak 'a' of the $\delta^{13}\text{C}_{\text{carb}}$ profile (Fig. 5), while its HO is recorded above 'a' in the classical C/T boundary reference sections (i.e., Pueblo: Kennedy et al., 2005; Caron et al., 2006; Eastbourne: Paul et al., 1999; Keller et al., 2001; Tsikos et al., 2004; Falzoni et al., 2018), and in nearby sections of the Vocontian Basin (e.g., Pont d'Issole: Grosheny et al., 2006; Jarvis et al., 2011). The HO of *Th. deecke* precedes the HO of *Th. greenhornensis* and both are recognized below peak 'a' in agreement with previous records (Paul et al., 1999; Caron et al., 2006; Grosheny et al., 2006; Wagreich et al., 2008; Bomou et al., 2013; Falzoni et al., 2008). However, litho- and chemostratigraphic correlation between Clot Chevalier and Pont d'Issole demonstrates that the level of rotaliporid extinction is a result of the combination of: 1) the presence of a hiatus at the base of Th1 and; 2) the presence of a condensed stratigraphic interval within Th1 and Th2 and; 3) palaeontological causes, namely the rare occurrence of rotaliporids at the top of their stratigraphic distribution. These facts likely biased the identification of their HOs (Falzoni et al., 2016b). The extinction level of *G. bentonensis* is fixed between the extinction level of *R. cushmani* (below) and peak B of the $\delta^{13}\text{C}$ profile (above), as recognized at Pueblo (Kennedy et

al., 2005), and Eastbourne (Paul et al. 1999). Thus, its HO might represent a very reliable bioevent to approximate the beginning of the $\delta^{13}\text{C}$ plateau and of the OAE 2 acme in the absence of geochemical markers. The LOs of *Dicarinella* species (i.e., *D. imbricata*, *D. elata*, *D. canaliculata*) and of *H. praehelvetica* are recognized to occur below peak A, as also found at Pueblo (Leckie, 1985; Caron et al., 2006; see $\delta^{13}\text{C}_{\text{org}}$ curve in Kennedy et al., 2005). However, these bioevents are absent or observed in different stratigraphic intervals in sections elsewhere (e.g., Eastbourne: Paul et al., 1999; Keller et al., 2001; Pont d'Issole: Grosheny et al., 2006) probably because of their rarity (*D. elata*, *D. canaliculata*) and/or transitional evolution from ancestor species (*D. imbricata*, *H. praehelvetica*). Significantly, the Clot Chevalier section reveals three planktonic foraminiferal bioevents falling slightly below (LO of *P. oraviensis*) and above (LO of *M. cf. schneegansi* and of *M. cf. sigali*) peak 'c', constraining the C/T boundary as defined by the C-isotope excursion relatively tightly. These bioevents appear particularly promising as aids to identification of the C/T boundary in the absence of the planktonic foraminiferal marker for the base of the Turonian *H. helvetica*, which is commonly absent or shows a diachronous LO (e.g., Kuhnt et al., 1997; Keller et al., 2001; Caron et al., 2006). In other pelagic sections of the Vocontian Basin, the LO of *H. helvetica* is recorded slightly above peak 'c' (Pont d'Issole: Grosheny et al., 2006; Jarvis et al., 2011; Falzoni et al., 2018) or where the $\delta^{13}\text{C}$ returns to pre-excursion values (Lambruisse: Takashima et al., 2009). Moreover, in these sections the LO of *H. helvetica* is recorded either a few metres below (Pont d'Issole) or above (Lambruisse) the appearance of the calcareous nannofossil *Q. gartneri*, further confirming the unreliability of *H. helvetica* as a marker for the base of the Turonian.

Calcareous nannofossil biostratigraphy has been used in several sections to characterize the Cenomanian–Turonian boundary interval and the OAE 2 carbon-isotope anomaly (Bralower, 1988; Nederbragt and Fiorentino 1999; Paul et al, 1999; Tsikos et al, 2004; Hardas and Mutterlose, 2006; Melinte-Dobrinescu and Bojar, 2008; Tantawy, 2008; Fernando et al, 2010; Linnert et al., 2010, 2011; Pavlishina and Wagreich, 2012; Corbett and Watkins 2013; Corbett et al., 2014). In the Clot Chevalier section, the nannofossil zonal and subzonal bioevents reported for the latest Cenomanian–earliest Turonian interval, and some secondary bioevents, have

been recognized. They are: the HO of *C. kennedyi*, LO of *R. biarcus*, HO of *L. acutus*, HO of *C. striatus*, HO of *A. albianus*, LO of *E. octopetalus*, HO of *H. chiastia*, LO of *Q. intermedium-5*, LO of *Q. gartneri* and LO of *E. moratus* (Fig. 5). However, *L. acutus* is sparse, *Q. intermedium-5* is extremely rare, and some bioevents were observed in a different order relative to the sequence of Burnett's (1998) zonation. Based on the comparison with published nannofossil biostratigraphies for the latest Cenomanian–earliest Turonian interval, our results support the highest reliability for the HOs of *C. kennedyi*, *A. albianus* and *H. chiastia*, and the LO of *Q. gartneri*. Moreover, the HO of *C. kennedyi* constrains the onset of the OAE 2 positive carbon-isotope anomaly, whereas the LO of *Q. gartneri* follows close on the end of the excursion (Fig. 5). It is important to underline that, in the Clot Chevalier section, specimens of *C. kennedyi*, *A. albianus* and *H. chiastia* are observed in samples above their normal HOs (Fig. 5), similar to records of other sections (e.g. Eastbourne: Linnert et al., 2010, 2011) for which re-sedimentation has been postulated. However, at Clot Chevalier, reworking is not supported by planktonic foraminiferal distribution.

Recent reinvestigation of the GSSP Pueblo section (Corbett et al., 2014) confirms that the base of the Turonian (LO of the ammonite *W. devonense*) is sandwiched between the HO of *H. chiastia* and LO of *Q. gartneri*. In particular, the LO of *Q. gartneri* shortly postdates the end of the positive shift (peak 'c') of the $\delta^{13}\text{C}$ curve and, as previously discussed by Tsikos et al. (2004), might be used to approximate the Cenomanian–Turonian boundary.

5.2 Palaeoceanography and palaeoclimate: the Plenus Cold Event

A feature of major palaeoceanographic interest revealed by study of this section is the Plenus Cold Event (PCE), which was originally recognized by Gale and Christensen (1996) based on macrofossil distribution and oxygen-isotope data from the Chalk of southern England and elsewhere. The concept arose from the discovery that the Cenomanian “North Boreal” fauna that Jefferies (1963) had described from the Plenus Marl Beds 4–6 in the Anglo-Paris Basin was coincident with a heavy oxygen-isotope excursion in bulk chalk (Lamolda et al., 1994). In detail, the PCE can locally be divided into two pulses of relative falls in temperature, including an earlier and less pronounced episode recorded in Bed 2 of the Plenus Marl in the Chalk of southern

England (Fig. 12 for section). Here, the interval recording the stratigraphically higher pulse correlates with a pronounced dip in the carbon-isotope curve that has proven to be a globally recognized feature and may record a decrease in the global sequestration of organic matter (Jenkyns et al., 2017).

Subsequently, the event was identified by the southerly spread of boreal dinocysts of the *Cyclonephelium compactum*–*membraniphorum* morphological plexus in the Western Interior Seaway (van Helmond et al. 2013, 2014; Eldrett et al. 2014). In the Atlantic, the event was identified from TEX₈₆ data in IODP Sites 367 (Cape Verde Basin) and 1260 (Demerara Rise), which suggested a temperature fall of ~4°C during the Plenus Cold Event for the equatorial Atlantic (Forster et al., 2007) and a larger drop of 5 to 11°C at Site 1276 in the Newfoundland Basin of the North Atlantic (Sinninghe Damsté et al., 2010). TEX₈₆ data from this level in the Bass River Borehole, New Jersey suggested a 2.5°C temperature fall (van Helmond et al., 2013) and 5°C at Wunstorf in northern Germany (van Helmond et al., 2015).

The event has also been identified from the presence of a drop of 1–2‰ in $\Delta^{13}\text{C}$ ($\delta^{13}\text{C}_{\text{carb}} - \delta^{13}\text{C}_{\text{org}}$) in Germany (Gröbern), south-east England (Eastbourne) and in the Vocontian Basin (Pont d'Issole), which has been interpreted, following Freeman and Hayes (1992), as due to a reduction in dissolved carbon dioxide and hence atmospheric $p\text{CO}_2$ (Jarvis et al. 2011). High-resolution $\Delta^{13}\text{C}$ and bulk oxygen-isotope data from the coeval organic-rich pelagic nannofossil carbonates of Tarfaya, Morocco similarly identify, respectively, a drop in dissolved CO_2 and a 3-stepped fall in temperature across the PCE interval (Kuhnt et al., 2017). Significantly, stomatal index data from leaves found in paralic facies situated palaeogeographically, over the same interval, at the edge of the Western Interior Seaway in North America (south-west Utah), indicate that the drop in $p\text{CO}_2$ was an atmospheric phenomenon and hence a global event (Barclay et al., 2010).

Previous evidence for the presence of the Plenus Cold Event in SE France was provided by the fauna of a single glauconitic bed in the section at Les Lattes, east of Castellane, and 35 km ESE of the Clot Chevalier outcrop (Fig. 1A; Gale and Christensen 1996; Grosheny et al. 2017). The Les Lattes section yielded typical boreal macrofaunal taxa, including *Oxytoma seminudum*, *Hamulus* sp., and *Praeactinocamax plenus*, all typical of Bed 4 of the Plenus Marl in the Anglo-Paris

Basin (Jefferies 1962, 1963). The section at Les Lattes comprises dominantly silty and sandy marls and completely lacks organic-rich levels and evidently represents significantly shallower water conditions to those developed to the north of Vergons (Fig. 1A, C; Grosheny et al. 2017).

Evidence for general re-oxygenation of the sea floor during the PCE derives from the spread of benthonic foraminifera in sediments recording the event and comes from multiple sites, including outcrops and cores from the Western Interior of North America, Demerara Rise in the western equatorial Atlantic, and Tarfaya, Morocco (Eicher and Worstell, 1970; Keller and Pardo, 2004; Kuhnt et al., 2005; Friedrich et al., 2006; Keller et al., 2008; Prokoph et al., 2013; Eldrett et al., 2014; Elderbak et al., 2014; Elderbak and Leckie, 2016).

The PCE interval at Clot Chevalier is approximately defined by the fall in carbon-isotope values, possibly also the relatively low TOC values and by an increase in oxygen-isotope values, albeit complicated by the condensed nature of this part of the section (Fig. 7). Its basal level is effectively constrained by the LO (Lowest Occurrence) of *R. biarcus*, and the top lies close to the HO (Highest Occurrence) of *L. acutus*, and the event falls within the uppermost part of the nannofossil zone NC11* including lithological units Th2 and the base of Th3 (Fig. 5). On the basis of nannofossil events, the biostratigraphic calibration of the PCE is similar to that at Eastbourne, Sussex, UK where *R. biarcus* first appears at the base of Bed 4 of the Plenus Marls (Erba, unpublished data), and the highest occurrence of *L. acutus* is found immediately above the top of this stratigraphic unit (Linnert et al., 2011).

The impact of the Plenus Cold Event at Clot de Chevalier is shown by a number of independent parameters. The stratigraphic record of $\Delta^{13}\text{C}_{\text{carb-TOC}}$ shows a fall of nearly 1.5‰ over the 2.5–7.0 m interval, overlapping lithological unit Th2, and can be interpreted as a signal of declining dissolved CO_2 (Figs 7, 11). The validity of this proxy is commonly limited due to variable sources and preservation of bulk organic matter, but the excellent correlation between the $\delta^{13}\text{C}$ of S-bound phytane and TOC ($R^2 = 0.91$, Table 3), suggests that $\delta^{13}\text{C}_{\text{TOC}}$ faithfully records primary water-column processes of organic carbon-isotope fractionation. Similarly, the positive $\delta^{18}\text{O}$ excursion of $\sim 1\%$ over the 3–7 m interval would translate into a fall in temperature of $\sim 4\text{--}5^\circ\text{C}$ consistent with a decrease in dissolved (and presumably

atmospheric) CO₂, assuming no major diagenetic overprint on the carbonate component (Fig. 7). A similar positive shift in bulk oxygen-isotope ratios is recorded from coeval sediments at Ondres, and coiling ratios in the planktonic foraminiferan *Muricohedbergella delrioensis* in correlative strata at Pont d'Issole also indicate cooling (Grosheny et al., 2017). These relationships suggest a tight linkage between dissolved CO₂ and local seawater temperature.

The oxygen-isotope trend at Clot Chevalier, the PCE interval excepted, suggests long-term warming extending into the Turonian, in common with many other sections of comparable age (Voigt et al., 2004; Friedrich et al., 2012; O'Brien et al., 2017).

Possible feedbacks increasing dissolved CO₂ in the water mass unrelated to temperature during the Plenus Cold Event can, however, also be envisaged. Cooling of surface waters would, of itself, have allowed incorporation of more dissolved carbon dioxide but more subtle effects may have been at work, independent of atmospheric pCO₂ and its exchange with surface waters. A significant increase in dissolved oxygen of ocean waters would have been brought about by cooling, which in turn apparently led to oxidation of previously deposited organic matter during the early stages of OAE 2 causing the transient release of many redox-sensitive and chalcophilic elements initially derived from basalt–seawater interaction during the PCE (Orth et al., 1993; Sinton and Duncan, 1997; Snow et al., 2005; Jenkyns et al., 2017; Clarkson et al., 2018; Sweere et al., 2018). Oxidation of this organic matter during the PCE would have added isotopically depleted dissolved CO₂ to the bottom waters, probably in addition to that volcanically or hydrothermally derived, as suggested by osmium-isotope profiles from many parts of the world (Turgeon and Creaser 2008; Du Vivier et al., 2015, 2016) and mercury anomalies from the Atlantic and Western Interior Seaway (Scaife et al., 2017). Changes in upwelling intensity of such a CO₂-rich water mass might well have influenced the composition of near-surface waters. Such phenomena, however, need to be placed in the context of the relative efficacy of sinks for this greenhouse gas due burial of organic matter and weathering of mafic and felsic rocks (e.g. Forster et al., 2007; Sinninghe Damsté et al., 2010; Blättler et al., 2011; Jarvis et al., 2011; Pogge von Strandmann, 2013; Jenkyns et al., 2017). The return from the cooler more oxygenated PCE to warmer

more anoxic conditions must indicate that sources outcompeted the sinks for CO₂ in the latter stages of OAE 2.

Overall, the PCE interval excepted, global drawdown of redox-sensitive species was a feature of OAE 2 due to the spread of anoxic–euxinic conditions, so that the marine pool of such trace elements was relatively depleted (van Bentum et al., 2009; Hetzel et al., 2009; Owens et al., 2016; Oet al., 2017). The peaks in Ni/Fe and Fe/Al (Fig. 9) correlate with the interval recording the Plenus Cold Event and may be a regional to global response to the prevailing redox conditions. Notably, Ni and Fe are concentrated, together with other redox-sensitive and chalcophilic geochemical species, at the level of the Plenus Cold Event in the Chalk of Eastbourne, southern England (Fig. 12; Jenkyns et al., 2017; Clarkson et al., 2018). In the case of Fe, the elevated levels of this element at Clot Chevalier must, at least in part, be due to the presence of glauconite, the grains of which characterize this part of the section. Appropriate redox conditions and metal content of seawater (relatively elevated content of dissolved ferrous iron and lack of sulfide), coupled with relatively slow rates of sedimentation for this part of the section (stratigraphically condensed Units Th1 and Th2), would have favoured formation of this mineral (Cloud, 1955; Jenkyns, 1980; Odin and Matter, 1981).

In summary, the Plenus Cold Event, and the geochemical changes associated therewith, reflects a natural feedback in the Earth's climatic system to the extremely high temperatures that characterized major Cretaceous Oceanic Anoxic Events (Jenkyns et al., 2017; O'Brien et al., 2017). The characteristic signature of the PCE, namely relatively elevated oxygen-isotope values of bulk carbonate indicating relatively low marine temperatures, a trough in the positive excursion of the carbonate carbon-isotope profile, possibly relatively low TOC values, and a drop in $\Delta^{13}\text{C}$ have all left their characteristic marks in the Cenomanian–Turonian sediments of Clot Chevalier.

Acknowledgements. C. Bottini and E. Erba were funded through SIR-2014 (Ministero dell'Istruzione, dell'Università e della Ricerca – Scientific Independence of young Researchers) to C. Bottini. F Falzoni and M.R. Petrizzo were funded by MIUR-PRIN 779 2010-2011 (2010X3PP8J_001) to Elisabetta Erba (scientific coordinator). JSSD

receives funding from the Netherlands Earth System Science Center (NESSC) through a gravitation grant (024.002.001) from the Dutch Ministry for Education, Culture and Science. We are grateful to the reviewers for many helpful comments.

References

- Algeo, T., Tribovillard, N., 2009. Environmental analysis of paleoceanographic systems based on molybdenum-uranium covariation. *Chemical Geology* **268**, 211–225.
- Arthur, M. A., Dean, W. E., Pratt, L. M., 1988. Geochemical and climatic effects of increased marine organic carbon burial at the Cenomanian/Turonian boundary. *Nature* **335**, 714–717.
- Arthur, M.A., Schlanger, S.O., Jenkyns, H.C., 1987. The Cenomanian–Turonian Oceanic Anoxic Event, II. Palaeoceanographic controls on organic-matter production and preservation. In: *Marine Petroleum Source Rocks* (Eds J. Brooks and A. J. Fleet), Special Publication Geological Society, London **26**, 401–420.
- Barclay, R.S., McElwain, J.C., Sageman, B.B., 2010. Carbon sequestration activated by a volcanic CO₂ pulse during Ocean Anoxic Event 2. *Nature Geoscience*, 3, 205–208.
- Batenburg, S.J., de Vleeschouwer, D., Sprovieri, M., Hilgen, F.J., Gale, A.S., Singer, B.S., Koeberl, C., Coccioni, R., Claeys, P., Montinari, A., 2016. Orbital control on the timing of oceanic anoxia in the Late Cretaceous. *Climate of the Past* **12**, 1995–2016.
- Behar, F., Beaumont, V., Penteado, H.D.B., 2001. Rock-Eval 6 technology: performances and developments. *Oil & Gas Science and Technology*, 56: 111–134.
- Blättler, C.L., Jenkyns, H.C., Reynard, L.M., Henderson, G.M., 2011. Significant increases in global weathering during Oceanic Anoxic Events 1a and 2 indicated by calcium isotopes. *Earth and Planetary Science Letters* **309**, 77–88.
- Bomou, B., Adatte, T., Tantawy, A.A., Mort, H., Fleitmann, D., Huang, Y., Föllmi, K.B., 2013. The expression of the Cenomanian–Turonian oceanic anoxic event in Tibet. *Palaeogeography, Palaeoclimatology, Palaeoecology* **369**, 466–481.
- Bralower, T.J., 1988. Calcareous nannofossil biostratigraphy and assemblages of the Cenomanian-Turonian boundary interval: implications for the origin and timing of oceanic anoxia. *Paleoceanography* **3**, 275–316

- Bralower, T.J., Leckie, R.M., Sliter, W.V., Thierstein, H.R., 1995. An integrated Cretaceous microfossil biostratigraphy. In: Berggren, W.A., Kent, D.V., Aubry, M.-P., Hardenbol, J. (Eds.), *Geochronology, Time Scales and Global Stratigraphic Correlation*. Society of Economic Paleontologists and Mineralogists, Special Publication **54**, 65–79.
- Brassell, S. C., Eglinton, G., Maxwell, J. R., & Philp, R. P., 1978. Natural background of alkanes in the aquatic environment. In: Hutzinger, O, Van Lelyveld, I.H., Zoetman, B.C.J. (eds). *Aquatic pollutants: Transformation and biological effects*, pp 69–86. Pergamon Press, Oxford.
- Burnett, J.A., 1998. Upper Cretaceous. In: Bown, P.R. (Eds.), *Calcareous nannofossil biostratigraphy*. Chapman and Hall, London, 132-199.
- Caron, M., Dall'Agnolo, S., Accarie, H., Barrera, E., Kauffman, E.G., Amédro, F., Robaszynski, F., 2006. High-resolution stratigraphy of the Cenomanian–Turonian boundary interval at Pueblo (USA) and Wadi Bahloul (Tunisia): stable isotope and bio-events correlation. *Geobios* **39**, 171–200.
- Clarke, L. J., Jenkyns, H.C., 1999. New oxygen isotope evidence for long-term Cretaceous climatic change in the Southern Hemisphere, *Geology* **27**, 699–702.
- Clarkson, M.O., Stirling, C.H., Jenkyns, H.C., Dickson, A.J., Porcelli, D., Moy, C.M., von Strandmann, P.A.P., Cooke, I.R., Lenton, T.M., 2018. Uranium isotope evidence for two episodes of deoxygenation during Oceanic Anoxic Event 2. *Proceedings of the National Academy of Sciences* **115**, 2918–2923.
- Cloud Jr, P.E., 1955. Physical limits of glauconite formation. *AAPG Bulletin* **39**, 484–492.
- Corbett, M.J., Watkins, D.K., 2013. Calcareous nannofossil paleoecology of the mid-Cretaceous Western Interior Seaway and evidence of oligotrophic surfacewaters during OAE2. *Palaeogeography, Palaeoclimatology, Palaeoecology* **392**, 510–523.
- Corbett, M.J., Watkins, D.K., Pospichal, J.J., 2014. A quantitative analysis of calcareous nannofossil bioevents of the Late Cretaceous (Late Cenomanian–Coniacian) Western Interior Seaway and their reliability in established zonation schemes. *Marine Micropaleontology* **109**, 30-45.
- Crumièrè, J. P., 1989. Crise anoxique à la limite Cénomanièn-Turonien dans le bassin subalpin oriental (sud-est de la France). Relation avec l'eustatisme, *Geobios Memoire Special* **22**, suppl. 1, 189–203.
- Crumièrè, J. P., Crumièrè-Airaud, C., Espitalié, J., Cotillon, P., 1990. Global and regional

- controls on potential source-rock deposition and preservation: The Cenomanian-Turonian Oceanic Anoxic Event (CTOAE) on the European Tethyan margin (southeastern France), in *Deposition of Organic Facies*, edited by A. Y. Huc, AAPG Stud. Geol., **30**, 107–118.
- Dickson, A.J., Jenkyns, H.C., Porcelli, D., van den Boorn, S., Idiz, E., 2016. Basin-scale controls on the molybdenum-isotope composition of seawater during Oceanic Anoxic Event 2 (Late Cretaceous). *Geochimica et Cosmochimica Acta* **178**, 291–306.
- Dickson, A.J., Saker-Clark, M., Jenkyns, H.C., Bottini, C., Erba, E., Russo, F., Gorbanenko, O., Naafs, B.D., Pancost, R.D., Robinson, S.A. and Boorn, S.H., 2017. A Southern Hemisphere record of global trace-metal drawdown and orbital modulation of organic-matter burial across the Cenomanian–Turonian boundary (Ocean Drilling Program Site 1138, Kerguelen Plateau). *Sedimentology* **64**, 186–203.
- Du Vivier, A., Selby, D., Sageman, B., Jarvis, I., Gröcke, D., Voigt, S., 2014. Marine $^{187}\text{Os}/^{188}\text{Os}$ isotope stratigraphy reveals the interaction of volcanism and ocean circulation during Oceanic Anoxic Event 2, *Earth and Planetary Science Letters* **389**, 23–33.
- Du Vivier, A.D.C., Selby, D., Condon, D.J., Takashima, R., Nishi, H., 2015. Pacific $^{187}\text{Os}/^{188}\text{Os}$ isotope chemistry and U–Pb geochronology: Synchronicity of global Os isotope change across OAE 2. *Earth and Planetary Science Letters* **428**, 204–216.
- Eicher, D.L., Worstell, P., 1970. Cenomanian and Turonian foraminifera from the Great Plains, United States. *Micropaleontology* **16**, 269–324.
- Elderbak, K., Leckie, R. M., Tibert, N. E., 2014. Paleoenvironmental and paleoceanographic changes across the Cenomanian–Turonian Boundary Event (Oceanic Anoxic Event 2) as indicated by foraminiferal assemblages from the eastern margin of the Cretaceous Western Interior Sea. *Palaeogeography, Palaeoclimatology, Palaeoecology* **413**, 29–48.
- Elderbak, K., Leckie, R. M., 2016. Paleocirculation and foraminiferal assemblages of the Cenomanian–Turonian Bridge Creek Limestone bedding couplets: Productivity vs. dilution during OAE2. *Cretaceous Research* **60**, 52–77.
- Eldrett, J. S., Minisini, D., Bergman, S.C., 2014. Decoupling of the carbon cycle during Oceanic Anoxic Event 2. *Geology* **42**, 567–570.
- Erbacher, J., Friedrich, O., Wilson, P.A., Birch, H. and Mutterlose, J., 2005. Stable organic carbon isotope stratigraphy across Oceanic Anoxic Event 2 of Demerara Rise,

- western tropical Atlantic. *Geochemistry, Geophysics, Geosystems* **6**, Q06010, doi: 10.1029/2004GC000850.
- Falzone F., Petrizzo M.R., Clarke L.J., MacLeod K.G., Jenkyns H.C., 2016a. Long-term Late Cretaceous oxygen- and carbon-isotope trends and planktonic foraminiferal turnover: A new record from the southern midlatitudes. *GSA Bulletin* **128**, 1725–1735.
- Falzone F., Petrizzo M.R., Jenkyns H.C., Gale A.S., Tsikos H., 2016b. Planktonic foraminiferal biostratigraphy and assemblage composition across the Cenomanian-Turonian boundary interval at Clot Chevalier (Vocontian Basin, SE France). *Cretaceous Research* **59**, 69–97.
- Falzone F., Petrizzo M.R., Caron M., Leckie R.M., Elderbak K., 2018. Age and synchronicity of planktonic foraminiferal bioevents across the Cenomanian–Turonian boundary interval (Late Cretaceous). *Newsletters on Stratigraphy*, doi: 10.1127/nos/2018/0416.
- Farrimond P., Eglinton G., Brassell S.C. and Jenkyns H.C., 1990. The Cenomanian/Turonian anoxic event in Europe: an organic geochemical study. *Marine and Petroleum Geology* **7**, 75–89.
- Fernando A.G.S., Takashima R., Nishi H., Giraud F., Okada H., 2010. Calcareous nannofossil biostratigraphy of the Thomel Level (OAE2) in the Lambruisse section, Vocontian Basin, southeast France. *Geobios* **43**, 45–57.
- Forster A., Schouten S., Moriya K., Wilson P.A., Sinninghe Damsté J.S., 2007. Tropical warming and intermittent cooling during the Cenomanian/Turonian oceanic anoxic event 2: Sea surface temperature records from the equatorial Atlantic. *Paleoceanography* **22**, PA1219, doi: 10.1029/2006PA001349.
- Freeman K.H. and Hayes J.M., 1992. Fractionation of carbon isotopes by phytoplankton and estimates of ancient CO² levels. *Global Biogeochemical Cycles* **62**, 185–198.
- Friedrich O., Erbacher J., Mutterlose J., 2006. Paleoenvironmental changes across the Cenomanian/Turonian Boundary Event (Oceanic Anoxic Event 2) as indicated by benthic foraminifera from the Demerara Rise (ODP Leg 207). *Revue de Micropaléontologie* **49**, 121–139.

- Friedrich, O., Norris, R.D., Erbacher, J., 2012. Evolution of middle to Late Cretaceous Oceans—A 55 m.y record of Earth's temperature and carbon cycle. *Geology* **40**, 107–110.
- Gale, A.S., 1995. Cyclostratigraphy and correlation of the Cenomanian of Europe. In House, M.R. and Gale A.S. (eds.), *Orbital forcing timescales and cyclostratigraphy*. Special Publications of the Geological Society, **85**, 177–197.
- Gale, A. S., Christensen, W.G., 1996. Occurrence of the belemnite *Actinocamax plenus* in the Cenomanian of SE France and its significance, *Bulletin of the Geological Society of Denmark* **43**, 68–77.
- Gale, A. S., Kennedy, W.J., Voigt, S., Walaszczyk, I., 2005. Stratigraphy of the Upper Cenomanian–Lower Turonian Chalk succession at Eastbourne, Sussex, UK: Ammonites, inoceramid bivalves and stable carbon isotopes. *Cretaceous Research* **26**, 460–487.
- Gale, A.S., Hancock, J.M., Kennedy W. J., 1999. Biostratigraphical and sequence correlation of the Cenomanian successions of Mangyshlak (Kazakhstan), Crimea (Ukraine) and southern England. *Bulletin de l'Institut Royal des Sciences Naturelles de Belgique. Sciences de la terre* **69**-supp.A, 67–86.
- Gambacorta, G., Jenkyns, H.C., Russo, F., Tsikos, H., Wilson, P.A., Faucher, G., Erba, E., 2015. Carbon- and oxygen-isotope records of mid-Cretaceous Tethyan pelagic sequences from the Umbria–Marche and Belluno Basins (Italy). *Newsletters on Stratigraphy* **48**, 299–323.
- Gradstein, F.M., Ogg, J.G., Schmitz, M.D., Ogg, G.M., 2012. *The Geologic Time Scale 2012*. Elsevier, Oxford, UK, p. 1144.
- Grosheny, D., Beaudoin, B., Morel, L., Desmares, D., 2006. High-resolution biostratigraphy and chemostratigraphy of the Cenomanian/Turonian boundary event in the Vocontian Basin, southeast France, *Cretaceous Research* **27**, 629–640.
- Grosheny, D., Ferry, S., Lécuyer, C., Thomas, A., Desmares, D. 2017. The Cenomanian-Turonian Boundary Event (CTBE) on the southern slope of the Subalpine Basin (SE France), and its bearing on a probable tectonic pulse on a larger scale. *Cretaceous Research* **72**, 39–65.
- Hardas, P., Mutterlose, J., 2006. Calcareous nannofossil biostratigraphy of the Cenomanian/Turonian boundary interval of ODP Leg 207 at the Demerara Rise.

- Revue de Micropaléontologie **49**, 165–179.
- Hetzel, A., Böttcher, M.E., Wortmann, U.G. and Brumsack, H.J., 2009. Paleo-redox conditions during OAE 2 reflected in Demerara Rise sediment geochemistry (ODP Leg 207). *Palaeogeography, Palaeoclimatology, Palaeoecology* **273**, 302–328.
- Hayes, J.M., Freeman, K.F., Popp, B.N., Hoham, C.H., 1990. Compound-specific isotopic analyses: A novel tool for reconstruction of ancient biogeochemical processes. *Organic Geochemistry* **16**, 1115–1128.
- Jarvis, I, Gale, A.S., Jenkyns, H.C., Pearce, M.A., 2006. Secular variation in Late Cretaceous carbon isotopes: a new $d^{13}C$ reference curve for the Cenomanian-Campanian, 99.6–70.6 myr. *Geological Magazine* **143**, 561-608.
- Jarvis, I., Lignum, J.S., Gröcke, D.R., Jenkyns, H.C., Pearce, M.A., 2011. Black shale deposition, atmospheric CO₂ drawdown and cooling during the Cenomanian-Turonian Oceanic Anoxic Event. *Paleoceanography* **26**, PA3201, doi: 10.1029/2010PA002081.
- Jefferies, R. P. S., 1962. The palaeoecology of the *Actinocamax plenus* subzone (lowest Turonian) in the Anglo-Paris Basin, *Palaeontology* **4**, 609–647.
- Jefferies, R.P.S., 1963. The stratigraphy of the *Actinocamax plenus* subzone (Turonian) in the Anglo-Paris Basin. *Proceedings of the Geologists' Association* **74**, 1–33.
- Jenkyns, H.C., 1980. Cretaceous anoxic events: from continents to oceans. *Journal of the Geological Society* **137**, 171–188.
- Jenkyns, H. C., 1988. The early Toarcian (Jurassic) anoxic event; stratigraphic, sedimentary and geochemical evidence. *American Journal of Science* **288**, 101–151.
- Jenkyns, H.C., 2003. Evidence for rapid climate change in the Mesozoic-Palaeogene greenhouse world. *Philosophical Transactions of the Royal Society Series A* **361**, 1885–1916.
- Jenkyns, H. C., 2010. Geochemistry of oceanic anoxic events, *Geochemistry, Geophysics, Geosystems* **11**, Q03004, doi:10.1029/2009GC002788.
- Jenkyns, H. C., Gale, A.S., Corfield, R.M., 1994. Carbon- and oxygen-isotope stratigraphy of the English Chalk and Italian Scaglia and its palaeoclimatic significance. *Geological Magazine* **131**, 1–34.
- Jenkyns, H.C., Matthews, A., Tsikos, H. Erel, Y., 2007. Nitrate reduction, sulfate reduction, and sedimentary iron isotope evolution during the Cenomanian-Turonian oceanic anoxic event. *Paleoceanography*, **22**, PA3208, doi: 10.1029/2006PA001355.

- Jenkyns, H.C., Dickson, A.J., Ruhl, M. and van den Boorn, S.H., 2017. Basalt–seawater interaction, the Plenus Cold Event, enhanced weathering and geochemical change: deconstructing Oceanic Anoxic Event 2 (Cenomanian–Turonian, Late Cretaceous). *Sedimentology* **64**, 16–43.
- Jones, C. E., Jenkyns, H. C., 2001 Seawater strontium isotopes, oceanic anoxic events and sea-floor hydrothermal activity in the Jurassic and Cretaceous. *American Journal of Science* **301**, 112–149.
- Keller, G., Pardo, A., 2004. Age and paleoenvironment of the Cenomanian–Turonian global stratotype section and point at Pueblo, Colorado. *Marine Micropaleontology* **51**, 95–128.
- Keller, G., Han, Q., Adatte, T., Burns, S., 2001. Paleoenvironment of the Cenomanian–Turonian transition at Eastbourne, England. *Cretaceous Research* **22**, 391–422.
- Keller, G., Adatte, T., Berner, Z., Chellai, E.H., Stueben, D., 2008. Oceanic events and biotic effects of the Cenomanian–Turonian anoxic event, Tarfaya Basin, Morocco. *Cretaceous Research* **29**, 976–994.
- Kennedy, W.J., Walaszczyk, I., Cobban, W.P., 2005. The Global Boundary Stratotype Section and Point for the base of the Turonian Stage of the Cretaceous: Pueblo, Colorado. U.S.A. *Episodes* **28**, 93–104.
- Kolonic, S., Sinninghe Damsté, J. S., Böttcher, M.E., Kuypers, M.M.M., Kuhnt, W., Beckmann, B., Wagner, G.S.T., 2002. Geochemical characterisation of Cenomanian/Turonian Black Shales from the Tarfaya Basin (SW Morocco): relationships between palaeoenvironmental conditions and early sulphurization of sedimentary organic matter. *Journal of Petroleum Geology* **25**, 325–350.
- Kuhnt, W., Nederbragt, A., Leine, L., 1997. Cyclicity of Cenomanian – Turonian organic-carbon-rich sediments in the Tarfaya Atlantic Coastal Basin (Morocco). *Cretaceous Research* **18**, 587–601.
- Kuhnt, W., Luderer, F., Nederbragt, S., Thurow, J., Wagner, T., 2005. Orbital-scale record of the late Cenomanian–Turonian oceanic anoxic event (OAE-2) in the Tarfaya Basin (Morocco). *International Journal of Earth Sciences* **94**, 147–159.
- Kuhnt, W., Holbourn, A.E., Beil, S., Aquit, M., Krawczyk, T., Flögel, S., Chellai, E. H., Jabour, H., 2017. Unraveling the onset of Cretaceous Oceanic Anoxic Event 2 in an extended sediment archive from the Tarfaya–Laayoune Basin, Morocco. *Paleoceanography* **32**,

923–946.

- Kuypers, M.M.M., Pancost, R.D. and Sinninghe Damsté, J.S., 1999. A large and abrupt fall in atmospheric CO₂ concentration during Cretaceous times. *Nature* **399**, 342–344.
- Kuypers M.M.M., Pancost R.D., Nijenhuis I.A. and Sinninghe Damsté J.S., 2002. Enhanced productivity led to increased organic carbon burial in the euxinic North Atlantic basin during the late Cenomanian oceanic anoxic event. *Paleoceanography* **17**, 1051, 10.1029/2000PA000569.
- Kuypers M.M.M., Lourens L., Rijpstra W.I.C., Pancost R.D., Nijenhuis I.A., and Sinninghe Damsté J.S., 2004. Orbital forcing of organic carbon burial in the proto-North Atlantic during Oceanic Anoxic Event 2. *Earth Planet. Sci. Lett.* **228**, 465–482.
- Kuypers, M.M.M., van Breugel, Y., Schouten, S., Erba, E., Sinninghe Damsté, J.S., 2004. N₂-fixing cyanobacteria supplied nutrient N for Cretaceous oceanic anoxic events. *Geology* **32**, 853–856.
- Lamolda, M.A., Gorostidi, A., Paul, C.R.C., 1994. Quantitative estimates of calcareous nanofossil changes across the Plenus Marls (latest Cenomanian), Dover, England: implications for the generation of the Cenomanian-Turonian Boundary Event. *Cretaceous Research* **15**, 143–164.
- Leckie, R.M., 1985. Foraminifera of the Cenomanian–Turonian boundary interval, Greenhorn Formation, Rock Canyon Anticline, Pueblo, Colorado. In: Pratt, L.M., Kauffman, E.G., Zelt, F.B. (Eds.), *Fine-grained Deposits and Biofacies of the Cretaceous Western Interior Seaway: Evidence of Cyclic Sedimentary Processes*, Field Trip Guidebook, vol. 4. Society of Economic Paleontologists and Mineralogists, 139–149.
- Lees, J.A., 2007. New and rarely reported calcareous nanofossils from the Late Cretaceous of coastal Tanzania: outcrop samples and Tanzania Drilling Project Sites 5, 9 and 15. *Journal of Nannoplankton Research* **29**, 39–65.
- Linnert, C., Mutterlose, J., Erbacher, J., 2010. Calcareous nanofossils of the Cenomanian/Turonian boundary interval from the Boreal Realm (Wunstorf, northwest Germany). *Marine Micropaleontology* **74**, 38–58.
- Linnert, C., Mutterlose, J., Mortimore, R., 2011. Calcareous nanofossils from Eastbourne (southeastern England) and the paleoceanography of the Cenomanian–Turonian boundary interval. *Palaios* **26**, 298–313.

- Linnert, C., Robinson, S.A., Lees, J.A., Bown, P.R., Rodríguez, I.P., Petrizzo, M.R., Falzoni, F., Littler, K., Arz, J.A., Russell, E.E., 2014. Evidence for global cooling in the Late Cretaceous. *Nature Communications* **5**, 4194, doi: 10.1038/ncomms5194.
- Martin, E.E., MacLeod, K.G., Berrocoso, A.J., Bourbon, E., 2012. Water mass circulation on Demerara Rise during the Late Cretaceous based on Nd isotopes. *Earth and Planetary Science Letters* **327**, 111–120.
- Melinte-Dobrinescu, M.C., Bojar, A.-V., 2008. Biostratigraphic and isotopic record of the Cenomanian-Turonian deposits in the Ohaba-Ponor section (SW Hateg, Romania). *Cretaceous Research* **29**, 1024–1034.
- Meyers, S.R., Siewert, S.E., Singer, B.S., Sageman, B.B., Condon, D.J., Obradovich, J.D., Jicha, B.R., Sawyer, D.A., 2012a. Intercalibration of radioisotopic and astrochronologic time scales for the Cenomanian–Turonian boundary interval, Western Interior Basin, USA. *Geology* **40**, 7–10.
- Meyers, S.R., Sageman, B.B., Arthur, M.A., 2012b. Obliquity forcing of organic matter accumulation during Oceanic Anoxic Event 2. *Paleoceanography* **27**, PA3212, doi: 10.1029/2012PA002286.
- Monechi, S., Thierstein, H., 1985. Late Cretaceous-Eocene nannofossil and magnetostratigraphic correlations near Gubbio, Italy. *Marine Micropaleontology* **9**, 419–440.
- Morel, L., 1998. Stratigraphie à haute resolution du passage Cénomanién-Turonien, Ph.D. thesis, 224 pp., Université de Paris VI Pierre et Marie Curie, Paris.
- Nederbragt, A.J., Fiorentino, A., 1999. Stratigraphy and palaeoceanography of the Cenomanian–Turonian Boundary Event in Oued Mellegue, north-western Tunisia. *Cretaceous Research* **20**, 47–62.
- O'Brien, C.L., Robinson, S.A., Pancost, R.D., Sinninghe Damsté, J.S., Schouten, S., Lunt, D.J., Alsenz, H., Bornemann, A., Bottini, C., Brassell, S.C., Farnsworth, A., Forster, A., Huber, B.T., Inglis, G.N., Jenkyns, H.C., Linnert, C., Littler, K., Markwick, P., McAnena, A., Mutterlose, J., Naafs, B.D.A., Püttmann, W., Sluijs, A., van Helmond, A.G.M., Vellekoop, J., Wagner, T. & Wrobel, N.E. 2017., Cretaceous sea-surface temperature evolution: Constraints from TEX₈₆ and planktonic foraminiferal oxygen isotopes. *Earth-Science Reviews* **172**, 224–247.
- Odin, G.S., Matter, A., 1981. De glauconarium origine. *Sedimentology* **28**, 611–641.

- Orth, C.J., Attrep Jr, M., Quintana, L.R., Elder, W.P., Kauffman, E.G., Diner, R., Villamil, T., 1993. Elemental abundance anomalies in the late Cenomanian extinction interval: a search for the source(s). *Earth and Planetary Science Letters*, **117**, 189–204.
- Ourisson, G., Albrecht, P., Rohmer M., 1979. The hopanoids: palaeochemistry and biochemistry of a group of natural products. *Pure and Applied Chemistry* **51**, 709–729.
- Owens, J.D., Reinhard, C.T., Rohrsen, M., Love, G.D. and Lyons, T.W., 2016. Empirical links between trace metal cycling and marine microbial ecology during a large perturbation to Earth's carbon cycle. *Earth and Planetary Science Letters* **449**, 407–417.
- Paul, C. R. C., Lamolda, M.A., Mitchell, S.F., Vaziri, M.R., Gorostidi, A., Marshall, J.D., 1999. The Cenomanian-Turonian boundary at Eastbourne (Sussex, UK): A proposed European reference section. *Palaeogeography, Palaeoclimatology, Palaeoecology* **150**, 83–121.
- Pavlishina, P., Wagreich, M., 2012. Biostratigraphy and paleoenvironments in a northwestern Tethyan Cenomanian-Turonian boundary section (Austria) based on palynology and calcareous nannofossils. *Cretaceous Research* **38**, 103–112.
- Perch-Nielsen, K., 1985. Mesozoic calcareous nannofossils. In: Bolli, H.M., Saunders, J.B., Perch-Nielsen, K. (Eds.), *Plankton Stratigraphy*. Cambridge University Press, Cambridge, 329–427.
- Philip, J. et al., 2000. Map 14: Late Cenomanian. In: Dercourt, J., et al. (Eds), *Atlas Peri-Tethys Palaeogeographical Maps*. Comm. de la Carte Geol. du Monde, Paris.
- Pogge von Strandmann, P. A. E., Jenkyns, H.C., Woodfine, R.G., 2013. Lithium isotope evidence for enhanced weathering during Oceanic Anoxic Event 2. *Nature Geoscience* **6**, 668–672.
- Prokoph, A., Babalola, L.O., El Bilali, H., Olagoke, S., Rachold, V., 2013. Cenomanian–Turonian carbon isotope stratigraphy of the Western Canadian Sedimentary Basin. *Cretaceous Research* **44**, 39–53.
- Scaife, J.D., Ruhl, M., Dickson, A.J., Mather, T.A., Jenkyns, H.C., Percival, L.M.E., Hesselbo, S.P., Cartwright, J., Eldrett, J.S., Bergman, S.C. and Minisini, D., 2017. Sedimentary mercury enrichments as a marker for submarine Large Igneous Province volcanism?

- Evidence from the Mid-Cenomanian Event and Oceanic Anoxic Event 2 (Late Cretaceous). *Geochemistry, Geophysics, Geosystems* **18**, 4253–4275.
- Schlanger, S.O., Arthur, M.A., Jenkyns, H.C., Scholle P.A., 1987. The Cenomanian–Turonian oceanic anoxic event, I. Stratigraphy and distribution of organic carbon-rich beds and the marine $d^{13}C$ excursion. In: *Marine Petroleum Source Rocks* (Eds J. Brooks and A. J. Fleet), Special Publication Geological Society, London **26**, 371–399.
- Scholle, P.A., Arthur, M.A. (1980) Carbon isotope fluctuations in Cretaceous pelagic limestones: potential stratigraphic and petroleum exploration tool. *AAPG Bulletin* **64**, 67–87.
- Scopelliti, G., Bellanca, A., Coccioni, R., Luciani, V., Neri, R., Baudin, F., Chiari, M., Marcucci, M., 2004. High-resolution geochemical and biotic records of the Tethyan ‘Bonarelli Level’ (OAE2, latest Cenomanian) from the Calabianca–Guidaloca composite section, northwestern Sicily, Italy. *Palaeogeography, Palaeoclimatology, Palaeoecology* **208**, 293–317.
- Sinninghe Damsté, J.S., Köster, J., 1998. A euxinic southern North Atlantic Ocean during the Cenomanian/Turonian oceanic anoxic event. *Earth and Planetary Science Letters* **158**, 165–173.
- Sinninghe Damsté J.S., Kok M., Köster J. and Schouten S., 1998. Sulfurised carbohydrates: An important sedimentary sink for organic carbon? *Earth and Planetary Science Letters* **164**, 7–13.
- Sinninghe Damsté, J.S., Kuypers, M.M.M., Schouten, S., Schulte, S. and Rullkötter, J., 2003. The lycopane/C31 n-alkane ratio as a proxy to assess palaeoxicity during sediment deposition. *Earth and Planetary Science Letters* **209**, 215–226.
- Sinninghe Damsté, J.S., Kuypers, M.M.M., Pancost, R.D., Schouten, S., 2008. The carbon isotopic response of algae, (cyano)bacteria, archaea and higher plants to the late Cenomanian perturbation of the global carbon cycle: insights from biomarkers in black shales from the Cape Verde Basin (DSDP Site 367). *Organic Geochemistry* **39**, 1703–1718.
- Sinninghe Damsté, J.S., van Bentum, E.C., Reichart, G.J., Pross, J., Schouten, S., 2010. A CO_2 decrease-driven cooling and increased latitudinal temperature gradient during the mid-Cretaceous Oceanic Anoxic Event 2. *Earth and Planetary Science Letters* **293**, 97–103.

- Sinninghe Damsté, J.S., Schouten, S., Volkman, J.K., 2014. C₂₇–C₃₀ neohop-13 (18)-enes and their saturated and aromatic derivatives in sediments: Indicators for diagenesis and water column stratification. *Geochimica et Cosmochimica Acta* **133**, 402–421.
- Sinton, C. W., Duncan R.A., 1997. Potential links between ocean plateau volcanism and global ocean anoxia at the Cenomanian-Turonian boundary. *Economic Geology* **92**, 836–842.
- Sissingh, W., 1977. Biostratigraphy of Cretaceous calcareous nannoplankton. *Geol. Mijnbouw* **56**, 37–65.
- Snow, L. J., Duncan, R.A., Bralower, T.J., 2005. Trace element abundances in the Rock Canyon Anticline, Pueblo, Colorado, marine sedimentary section and their relationship to Caribbean plateau construction and oxygen anoxic event 2. *Paleoceanography* **20**, PA3005, doi:10.1029/2004PA001093.
- Sweere, T.C., Dickson, A.J., Jenkyns, H.C., Porcelli, D., Elrick, M., van den Boorn, H.J.M., Henderson, G.M., 2018. Isotopic evidence for changes in the zinc cycle during Oceanic Anoxic Event 2 (Late Cretaceous). *Geology* **45**, 463–466.
- Takashima, R., Nishi, H., Hayashi, K., Okada, H., Kawahata, H., Yamanaka, T., Fernando, A.G., Mampuku, M., 2009. Litho-, bio- and chemostratigraphy across the Cenomanian/Turonian boundary (OAE 2) in the Vocontian Basin of southeastern France, *Palaeogeography, Palaeoclimatology, Palaeoecology* **273**, 61–74.
- Tantawy, A.A., 2008. Calcareous nannofossil biostratigraphy and paleoecology of the Cenomanian – Turonian transition at Tazra, Tarfaya Basin, southern Morocco. *Cretaceous Research* **29**, 995-1007.
- Tribovillard, N., Algeo, T.J., Lyons T.W., Riboulleau A., 2006. Trace metals as palaeoredox and palaeoproductivity proxies: an update. *Chemical Geology* **232**, 12–32.
- Tribovillard, N., Algeo, T.J., Baudin, F., Riboulleau, A., 2012. Analysis of marine environmental conditions based on molybdenum–uranium covariation—Applications to Mesozoic paleoceanography. *Chemical Geology* **324**, 46–58.
- Tsikos, H., Jenkyns, H. C., Walsworth-Bell, B., Petrizzo, M. R., Forster, A., Kolonic, S., Erba, E., Premoli Silva, I., Baas, M., Wagner, T., Sinninghe Damsté, J.S., 2004. Carbon-isotope stratigraphy recorded by the Cenomanian–Turonian Oceanic Anoxic Event: correlation and implications based on three key localities. *Journal of the Geological Society* **161**, 711-719.

- Turgeon, S., Brumsack H.J., 2006. Anoxic vs dysoxic events reflected in sediment geochemistry during the Cenomanian-Turonian Boundary Event (Cretaceous) in the Umbria-Marche Basin of central Italy. *Chemical Geology* **234**, 321–339.
- Turgeon, S. C., Creaser, R.A., 2008. Cretaceous oceanic anoxic event 2 triggered by a massive magmatic episode. *Nature* **454**, 323–326.
- Valisolalao, J., Perakis, N., Chappe, B., Albrecht, P., 1984. A novel sulfur-containing C35 hopanoid in sediments. *Tetrahedron Letters* **25**, 1183–1186.
- van Bentum, E.C., Hetzel, A., Brumsack, H.J., Forster, A., Reichart, G.J. and Sinninghe Damsté, J.S., 2009. Reconstruction of water column anoxia in the equatorial Atlantic during the Cenomanian–Turonian oceanic anoxic event using biomarker and trace metal proxies. *Palaeogeography, Palaeoclimatology, Palaeoecology* **280**, 489–498.
- van Bentum E., Reichart G.-J., Sinninghe Damsté J.S., 2012. Organic matter provenance, paleoproductivity and bottom water ventilation during the Cenomanian/Turonian Oceanic Anoxic Event in the Newfoundland Basin. *Organic Geochemistry* **50**, 11–18.
- van Helmond, N.A.G.M., Sluijs, A., Reichart, G.-J., Sinninghe Damsté, J.S., Slomp, C.P. and Brinkhuis, H., 2013. A perturbed hydrological cycle during Oceanic Anoxic Event 2. *Geology* **42**, 123–126.
- van Helmond, N.A.G.M., Ruvalcaba, I., Sluijs, A., Sinninghe Damsté, J.S., and Slomp, C.P., 2014. Spatial extent and degree of oxygen depletion in the deep proto-North Atlantic basin during Oceanic Anoxic Event 2. *Geochemistry, Geophysics, Geosystems* **15**, 4254–4266.
- van Helmond, N.A.G.M., Sluijs, A., Sinninghe Damsté, J.S., Reichart G.-J., Voigt, S., Erbacher, J., Pross, J., Brinkhuis, H., 2015. Freshwater discharge controlled deposition of Cenomanian-Turonian black shales on the NW European continental shelf (Wunstorf, N Germany). *Climate of the Past*, **11**, 495–508.
- Voigt S, Gale AS, Flögel S. 2004 Midlatitude shelf seas in the Cenomanian-Turonian greenhouse world: Temperature evolution and North Atlantic circulation. *Paleoceanography* **19**, PA4020, doi: 10.1029/2004PA001015.
- Voigt, S., Gale, A. S., Voigt, T., 2006. Sea-level change, carbon cycling and palaeoclimate during the Late Cenomanian of northwest Europe; An integrated palaeoenvironmental analysis, *Cretaceous Research* **27**, 836–858.
- Voigt, S., Aurag, A., Leis, F., Kaplan, U., 2007. Late Cenomanian to Middle Turonian high-

- resolution carbon isotope stratigraphy: New data from the Münsterland Cretaceous Basin, Germany. *Earth and Planetary Science Letters* **253**, 196–210.
- Voigt, S., Erbacher, J., Mutterlose, J., Weiss, W., Westerhold, T., Wiese, F., Wilmsen, M., Wonik, T., 2008. The Cenomanian–Turonian of the Wunstorf section (north Germany): global stratigraphic reference section and new orbital time scale for oceanic anoxic event 2. *Newsletters on Stratigraphy* **43**, 65–89.
- Volkman, J. K., Barrett, S. M., Blackburn, S. I., Mansour, M. P., Sikes, E. L., Gelin, F., 1998. Microalgal biomarkers: a review of recent research developments. *Organic Geochemistry* **29**, 1163–1179.
- Wagreich, M., Bojar, A.-V., Sachsenhofer, R.F., Neuhuber, S., Egger, H., 2008. Calcareous nannoplankton, planktonic foraminiferal, and carbonate carbon isotope stratigraphy of the Cenomanian–Turonian boundary section in the Ultrahelvetetic Zone (Eastern Alps, Upper Austria). *Cretaceous Research* **29**, 965–975.
- Wedepohl, K. H. (1971). Environmental influences on the chemical composition of shales and clays. *Physics and Chemistry of the earth*. L. H. Ahrens, F. Press, S. K. Runcorn and H. C. Urey. Oxford, Pergamon: 305–333.
- Wedepohl, K. H. (1991). The composition of the upper Earth's crust and the natural cycles of selected metals. *Metals and their compounds in the environment*. In: E. Merian (editor), VCH-Verlagsgesellschaft, Weinheim, 3–17.
- Werne, J.P., Hollander, D.J., Behrens, A., Schaeffer, P., Albrecht, P., Sinninghe Damsté, J.S., 2000. Timing of early diagenetic sulfurization of organic matter: a precursor-product relationship in Holocene sediments of the anoxic Cariaco Basin, Venezuela. *Geochimica et Cosmochimica Acta* **64**, 1741–1751.
- Wray, D. S., Wood, C.J., 1998. Distinction between detrital and volcanogenic clay rich beds in Turonian-Coniacian chinks of eastern England. *Proceedings of the Yorkshire Geological Society* **52**, 95–105.
- Zheng, X.-Y., Jenkyns, H.C., Gale, A.S., Ward, D.J., Henderson, G.M., 2013. Changing ocean circulation and hydrothermal inputs during Ocean Anoxic Event 2 (Cenomanian–Turonian): evidence from Nd-isotopes in the European shelf sea. *Earth and Planetary Science Letters* **375**, 338–348.
- Zheng, X.-Y., Jenkyns, H.C., Gale, A.S., Ward, D.J., Henderson, G.M., 2016. A climatic control on reorganization of ocean circulation during the mid-Cenomanian event and

Cenomanian-Turonian oceanic anoxic event (OAE 2): Nd isotope evidence. *Geology* **44**. 151–154.

Figure captions.

Figure 1. A. Map to show position, indicated by stars, of sections described within the Vocontian Basin, as well as other localities referred to in the text, and location within France: after Crumière (1989), Crumière et al. 1990 and Falzoni et al., 2016). B. Palaeogeography of the northern Tethyan margin during the late Cenomanian, to show shorelines and major structural features: after Philip et al., 2000, Jarvis et al., 2011 and Falzoni et al., 2016b. C. Detailed palaeogeography of the Vocontian Basin, to show facies development: after Crumière et al., 1990. The Clot Chevalier section lies some 15 km to the west–north-west of the Vergons section at the edge of the realm of the so-called black shales.

Figure 2. Map of the region of St.-Lions, near Barreme, to show position of the Clot Chevalier section.

Figure 3. A. Map of eastern part of Vocontian Basin, to show positions of five described sections exposing the Niveau Thomel, and the Cenomanian–Turonian boundary. B. proposed correlation of these sections: Ondres (1), Pont d’Issole (2), Lambruisse (3), Clot Chevalier (4), and Vergons (5). Note that the Holywell Event was recognized and named by Jarvis et al. (2006) for a short-lived positive excursion of approximately 0.5–0.7‰ within the lowermost Turonian succession (level of Holywell Marls 3–4) in the Chalk deposits of southern England. The event is distinctive because it occurs during a period in which $\delta^{13}\text{C}$ values display an overall falling trend. Correlation based on stratigraphic and isotopic data from Grosheny et al. (2006), Takashima et al. (2009), Jarvis et al. (2011) and personal observations.

Fig. 4. Photograph of part of the Clot Chevalier section, with two marker bed turbidites indicated.

Fig. 5. Litho-, bio- and chemostratigraphic synthesis of the Clot Chevalier section. Calcareous nannofossil bioevents, distribution and relative abundance of selected marker species are reported. Nannofossil biozones: CC is after Sissingh (1977) as implemented by Perch-Nielsen (1985); NC is after Bralower et al. (1995), UC is after Burnett (1998) and NC** is after revision by Gambacorta et al. (2015).

Nannofossil assemblages A to C are based on semi-quantitative abundances. Abbreviations: Th1 to Th4 = lithological units belonging to the Thomel level. Planktonic foraminifera and carbonate carbon-isotope data according to Falzoni et al. (2016b). Key features on the carbon-isotope curve ('a', 'b', 'c') follow Voigt et al. (2007). The suggested OAE 2 interval stretches from the point of initial rise in carbon-isotope values to a level a little higher than peak 'c', beyond which $\delta^{13}\text{C}_{\text{carb}}$ falls below 4‰.

Fig. 6. (1) *Rucinolithus terebrodentarius*, sample SLT 1260. (2) *Tranolithus minimus*, sample SLT 360. (3) *Axopodorhabdus albianus*, sample SLT 180. (4) *Biscutum constans*, sample SLT180. (5) *Braarudosphaera regularis*, sample SLT 180. (6) *Aspidolithus enormis*, sample SLT 1260. (7) *Aspidolithus furtivus*, sample SLT 180. (8) *Calcioselenia fossilis*, sample SLT 2550. (9) *Corollithion kennedyi*, sample SLT 2550. (10) *Cretarhabdus striatus*, sample SLT 570. (11) *Cribrosphaerella ehrenbergii*, sample SLT 1470. (12) *Cyclagelosphaera rotaclypeata*, sample SLT 2880. (13) *Discorhabdus ignotus*, sample SLT 1260. (14) *Eiffellithus turriseiffelii*, sample SLT 1260. (15) *Eprolithus floralis*, sample SLT 2550. (16) *Eprolithus moratus*, sample SLT 2490. (17) *Eprolithus octopetalus*, sample SLT 2670. (18) *Helenea chiastia*, sample SLT 360. (19) *Lapideacassis mariae*, sample SLT 570. (20) *Lithraphidites acutus*, sample SLT 270. (21) *Owenia hillii*, sample SLT 180. (22) *Owenia hillii* (side view), sample SLT 180. (23) *Quadrum gartneri*, sample SLT 180. (24) *Quadrum intermedium-5*, sample SLT 3090. (25) *Quadrum intermedium-5*, same specimen. (26) *Rhagodiscus asper*, sample SLT 360. (27) *Rotelapillus biarcus*, sample SLT 1260. (28) *Sollasites horticus*, sample SLT 180. (29) *Watznaueria barnesiae*, sample SLT 570. (30) *Zeugrhabdotus bicrescenticus*, sample SLT 570. Scale bar = 5 μm .

Fig. 7. Plot of TOC, $\delta^{13}\text{C}_{\text{carb}}$, $\delta^{13}\text{C}_{\text{org}}$, $\delta^{13}\text{C}_{\text{carb}} - \delta^{13}\text{C}_{\text{org}}$ and $\delta^{18}\text{O}_{\text{carb}}$ for the Clot de Chevalier section. Note the 1.5‰ decrease in $\delta^{13}\text{C}_{\text{carb}} - \delta^{13}\text{C}_{\text{org}}$ over the 3m–7m interval denoting a possible fall in dissolved and atmospheric CO_2 and corresponding heavy $\delta^{18}\text{O}$ excursion ($\sim 4\text{--}5^\circ\text{C}$ temperature drop) which represents the Plenus Cold Event (PCE) and is used to plot its position in the section. Note also the relatively low TOC contents of the sediments over this interval, and dip in $\delta^{13}\text{C}_{\text{carb}}$, which likely reflect a drop in global deposition of organic matter (in this instance seen locally in

the Clot Chevalier section) under cooler and more oxygenated marine conditions (Jenkyns et al., 2017). Key features on the carbon-isotope curve ('a', 'b', 'c') follow Voigt et al. (2007). Legend as in Fig. 5.

Fig. 8. A. A pseudo-van Krevelen plot derived from Rock-Eval measurements, which indicates that the kerogen is best characterized as a degraded type II material with possible admixture of terrestrial higher plant debris. B. A stratigraphic plot of Oxygen Index (OI) and total organic carbon (TOC) again derived from Rock-Eval measurements, which shows a gradual decrease in OI values up-section to 1400 cm, possibly reflecting the incorporation of a higher proportion of marine-derived organic matter in the sediment.

Fig. 9. Stratigraphic profiles of bulk-rock isotopic (carbonate carbon and oxygen; TOC) and selected geochemical parameters (Fe/Al ratio; enrichment factors for Ni, V, Mo & U) for the Clot Chevalier section. Note relative enrichment of Fe/Al and relatively elevated nickel enrichment factors (EF) corresponding with the stratigraphic interval of the Plenian Cold Event (PCE) probably reflecting enhanced quantities of these redox-sensitive metals in global seawater derived from basalt–seawater interaction (Jenkyns et al., 2017). Legend as in Fig. 5.

Fig. 10. A cross-plot of Mo and U enrichment factors (Mo-EF and U-EF respectively; after Algeo and Tribovillard, 2009). Enrichment factors plot on an unrestricted marine trend. The diagonal lines represent multiples (0.1x, 0.3x and 1x) of the Mo:U mol:mol ratio of modern sea water (SW, ~7.5), converted to an equivalent sedimentary mass ratio (~3). UM represents the unrestricted marine trend of modern systems ranging from suboxic (bottom left) to anoxic (central upper region of the shaded area). PS represents the 'particulate shuttle' region characteristic of depositional basins which have intense redox cycling of metals (Algeo and Tribovillard, 2009; Tribovillard et al. 2012).

Fig. 11. Bulk-rock and corresponding compound-specific stratigraphic isotopic relationships for a selected sub-set of the 17 most organic-rich samples of the Clot Chevalier Cenomanian–Turonian section. The proxy for dissolved CO₂ $\Delta^{13}\text{C}$ ($\delta^{13}\text{C}_{\text{carb}}$ - $\delta^{13}\text{C}_{\text{org}}$) implies a drop in the concentration of this greenhouse gas at least during the interval recorded by the stratigraphic interval 3–7 m, and shows good agreement with the bulk oxygen-isotope record (Fig. 7) indicating the fall in seawater

temperature used to denote the stratigraphic position of the Plenus Cold Event (PCE). Legend as in Fig. 5.

Fig. 12. Fe/Ca and Ni/Ca ratios from the English Chalk at Eastbourne, Sussex plotted against the carbon-isotope record, the Plenus Cold Event and the proposed interval affected by the mafic/volcanic/hydrothermal episode. Proposed OAE interval is given by the grey band. The elemental 'spikes' in Fe and Ni correlate with the interval of the Plenus Cold Event, during which the global area of anoxic sinks for redox-sensitive and chalcophilic species would have been reduced and oxidation of previously deposited organic matter and pyrite could have liberated many metal elements. Ongoing basalt-seawater interaction would also have introduced metal ions that potentially remained in seawater at this time. Analytical details in Jenkyns et al. (2017).

Table captions

Table 1 (a, b). Calcareous nannofossil stratigraphic distribution and biozonation

Table 2. Calcareous plankton bioevents recorded in the Clot Chevalier section. Calcareous nannofossil bioevents are from this work, planktonic foraminiferal bioevents are according to Falzoni et al. (2016b). LO = Lowest Occurrence; HO = Highest Occurrence

Table 3. R2 values for the linear correlations between the $\delta^{13}\text{C}$ values of carbonate, TOC, and biomarkers

Taxonomic Appendix

Calcareous nannofossils

Calcareous nannofossil species identified and reported in the distribution chart (Table 1) are here listed following genera and species alphabetical order.

Genus *Ahmuellerella* Reinhardt, 1964

A. octoradiata (Górka, 1957) Reinhardt & Górka, 1967

Genus *Amphizygus* Bukry, 1969

A. brooksii Bukry, 1969

Genus *Aspidolithus* Noël, 1969

A. enormis (Shumenko, 1968) Manivit, 1971

A. furtivus (Bukry, 1969) Perch-Nielsen, 1984

Genus *Axopodorhabdus* Wind & Wise in Wise & Wind, 1977

A. albianus (Black, 1967) Wind & Wise in Wise & Wind, 1977

Genus *Biscutum* Black in Black & Barnes, 1959

B. constans (Górka, 1957) Black in Black and Barnes, 1959

Genus *Braarudosphaera* Deflandre, 1947

B. regularis Black, 1973

Genus *Broinsonia* Bukry, 1969

B. matalosa (Stover, 1966) Burnett in Gale et al., 1996

B. signata (Noël, 1969) Noël, 1970

Genus *Bukrylithus* Black, 1971

B. ambiguus Black, 1971

Genus *Calciosolenia* Gran, 1912

C. fossilis (Deflandre in Deflandre & Fert, 1954) Bown in Kennedy et al., 2000

Genus *Calculites* Prins & Sissingh in Sissingh, 1977

C. percernis Jeremiah, 1996

Genus *Chiastozygus* Gartner, 1968

C. amphipons (Bramlette & Martini, 1964) Gartner, 1968

C. bifarius Bukry, 1969

C. litterarius (Górka, 1957) Manivit, 1971

C. platyrhethus Hill, 1976

Genus *Corollithion* Stradner, 1962

C. exiguum Stradner, 1961

C. kennedyi Crux, 1981

C. madagaskarensis Perch-Nielsen, 1973

C. signum Stradner, 1963

Genus *Cretarhabdus* Bramlette & Martini, 1964

C. conicus Bramlette & Martini, 1964

C. striatus (Stradner, 1963) Black, 1973

Genus *Cribrosphaerella* Deflandre in Piveteau, 1952

C. ehrenbergii (Arkhangelsky, 1912) Deflandre in Piveteau, 1952

Genus *Cyclagelosphaera* Noël, 1965

C. reinhardtii (Perch-Nielsen, 1968) Romein, 1977

C. rotaclypeata Bukry, 1969

Genus *Cylindralithus* Bramlette & Martini, 1964

C. nudus Bukry, 1969

C. sculptus Bukry, 1969

Genus *Discorhabdus* Noël, 1965

D. ignotus (Górka, 1957) Perch-Nielsen, 1968

Genus *Eiffellithus* Reinhardt, 1965

E. gorkae Reinhardt, 1965

E. keio Shamrock in Shamrock and Watkins, 2009

E. perch-nielseniae Shamrock in Shamrock & Watkins, 2009

E. turriseiffelii (Deflandre in Deflandre & Fert, 1954) Reinhardt, 1965

Genus *Eprolithus* Stover, 1966

E. apertior Black, 1973
E. moratus (Stover, 1966) Burnett in Burnett et al., 1998
E. floralis (Stradner, 1962) Stover, 1966
E. octopetalus Varol, 1992
Genus *Flebellites* Thierstein, 1973
F. oblongus (Bukry, 1969) Crux in Lord, 1982
Genus *Gartnerago* Bukry, 1969
G. margaritatus Blair & Watkins, 2009
G. segmentatum (Stover, 1966) Thierstein, 1974
Genus *Gorkaea* Varol & Girgis, 1994
G. pseudanthophorus (Bramlette & Martini, 1964) Varol & Girgis, 1994
Genus *Grantarhabdus* Black, 1971
G. coronadventis (Reinhardt, 1966) Grün in Grün and Allemann, 1975
Genus *Haqius* Roth, 1978
H. circumradiatus (Stover, 1966) Roth, 1978
Genus *Helenea* Worsley, 1971
H. chiastia Worsley, 1971
Genus *Helicolithus* Noël, 1970
H. anceps (Górka, 1957) Noël, 1970
H. compactus (Bukry, 1969) Varol & Girgis, 1994
H. trabeculatus (Górka, 1957) Verbeek, 1977
H. turonicus Varol & Girgis, 1994
Genus *Lepideacassis* Black, 1971
L. mariae (Black, 1971) Wind & Wise in Wise & Wind, 1977
Genus *Lithastrinus* Stradner, 1962
L. quadricuspis Farhan, 1987
Genus *Lithraphidites* Deflandre, 1963
L. acutus Verbeek & Manivit in Manivit et al., 1977
L. carniolensis Deflandre, 1963
Genus *Loxolithus* Noël, 1965
L. armilla (Black in Black & Barnes, 1959) Noel, 1965
Genus *Manivitella* Thierstein, 1971

- M. pemmatoidea* (Deflandre in Manivit, 1965) Thierstein, 1971
- Genus *Microrhabdulus* Deflandre, 1959
- M. belgicus* Hay & Towe, 1963
- M. decoratus* Deflandre, 1959
- Genus *Nannoconus* Kamptner, 1931
- Genus *Octocyclus* Black, 1972
- O. reinhardtii* (Bukry, 1969) Wind & Wise in Wise & Wind, 1977
- Genus *Owenia* Crux, 1991
- O. hillii* Crux, 1991
- Genus *Placozygus* Hoffman, 1970
- P. fibuliformis* (Reinhardt, 1964) Hoffman, 1970
- Genus *Prediscosphaera* Vekshina, 1959
- P. columnata* (Stover, 1966) Perch-Nielsen, 1984
- P. cretacea* (Arkhangelsky, 1912) Gartner, 1968
- P. ponticula* (Bukry, 1969) Perch-Nielsen, 1984
- P. spinosa* (Bramlette & Martini 1964) Gartner 1968
- Genus *Quadrum* Prins & Perch-Nielsen in Manivit et al., 1977
- Q. eneabrachium* Varol, 1992
- Q. gartneri* Prins & Perch-Nielsen in Manivit et al., 1977
- Q. intermedium* Varol, 1992
- Genus *Radiolithus* Stover, 1966
- R. planus* Stover, 1966
- R. undosus* (Black, 1973) Varol, 1992
- Genus *Retecapsa* Black, 1971
- R. angustiforata* Black, 1971
- R. crenulata* (Bramlette & Martini, 1964) Grün in Grün and Allemann, 1975
- R. ficula* (Stover, 1966) Burnett, 1997
- R. surirella* (Deflandre & Fert, 1954) Grün in Grün and Allemann, 1975
- Genus *Rhagodiscus* Reinhardt, 1967
- R. achlyostaurion* (Hill, 1976) Doeven, 1983
- R. angustus* (Stradner, 1963) Reinhardt, 1971
- R. asper* (Stradner, 1963) Reinhardt, 1967

- R. reniformis* Perch-Nielsen, 1973
- R. splendens* (Deflandre, 1953) Verbeek, 1977
- Genus *Rotelapillus* Noël, 1973
- R. biarcus* (Bukry, 1969) Lees & Bown, 2006
- R. crenulatus* (Stover, 1966) Perch-Nielsen, 1984
- Genus *Rucinolithus* Stover, 1966
- R. terebrodentarius* Applegate, Bralower, Covington and Wise, 1987
- Genus *Sollasites* Black, 1967
- S. horticus* (Stradner et al. in Stradner & Adamiker, 1966) Cepek & Hay, 1969
- Genus *Staurolithites* Caratini, 1963
- S.? aenigma* Burnett, 1997
- S. ellipticus* (Gartner, 1968) Lambert, 1987
- S. flavus* Burnett, 1997
- S. halfanii* Lees, 2007
- S. laffittei* Caratini, 1963
- Genus *Stoverius* Perch-Nielsen, 1984
- S. achylosus* (Stover, 1966) Perch-Nielsen, 1984
- Genus *Tegumentatum* Thierstein in Roth & Thierstein, 1972
- T. stradneri* Thierstein in Roth & Thierstein, 1972
- Genus *Tetrapodorhabdus* Black, 1971
- T. decorus* (Deflandre in Deflandre & Fert, 1954) Wind & Wise in Wise & Wind, 1977
- Genus *Tranolithus* Stover, 1966
- T. gabalus* Stover, 1966
- T. minimus* (Bukry, 1969) Perch-Nielsen, 1984
- T. orionatus* Reinhardt, 1966
- T. salillum* (Noel, 1965) Crux, 1981
- Genus *Watznaueria* Reinhardt, 1964
- W. barnesiae* (Black, 1959) Perch-Nielsen, 1968
- W. biporta* Bukry, 1969
- W. fossacinta* (Black, 1971) Bown in Bown & Cooper, 1989
- W. manivitiaie* Bukry, 1973

W. ovata Bukry, 1969

Genus *Zeugrhabdotus* Reinhardt, 1965

Z. acanthus Reinhardt, 1965

Z. bicrescenticus (Stover, 1966) Burnett in Gale et al., 1996

Z. biperforatus (Gartner, 1968) Burnett, 1997

Z. diplogrammus (Deflandre in Deflandre & Fert, 1954) Burnett in Gale et al.,
1996

Z. embergeri (Noël, 1958) Perch-Nielsen, 1984

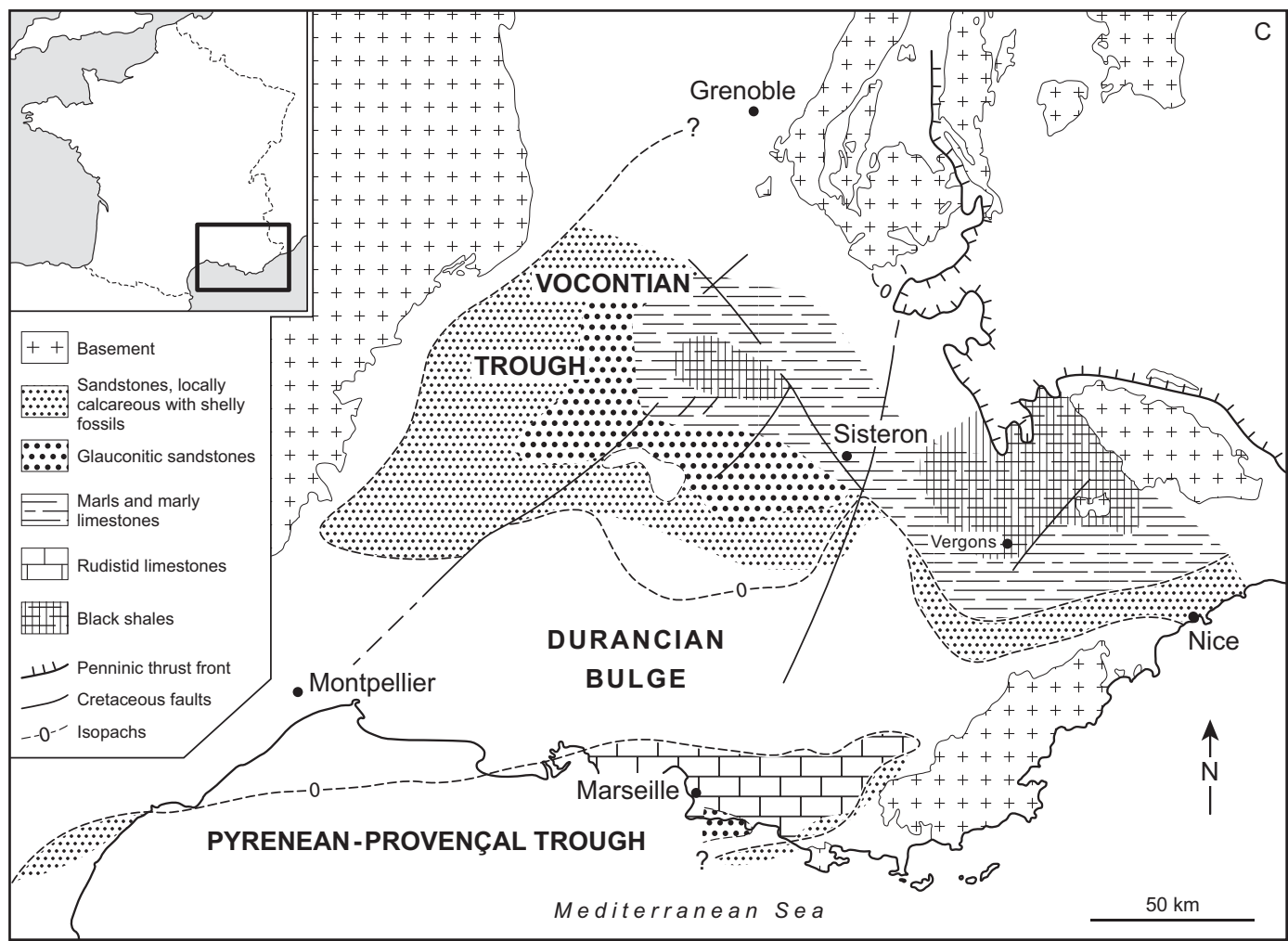
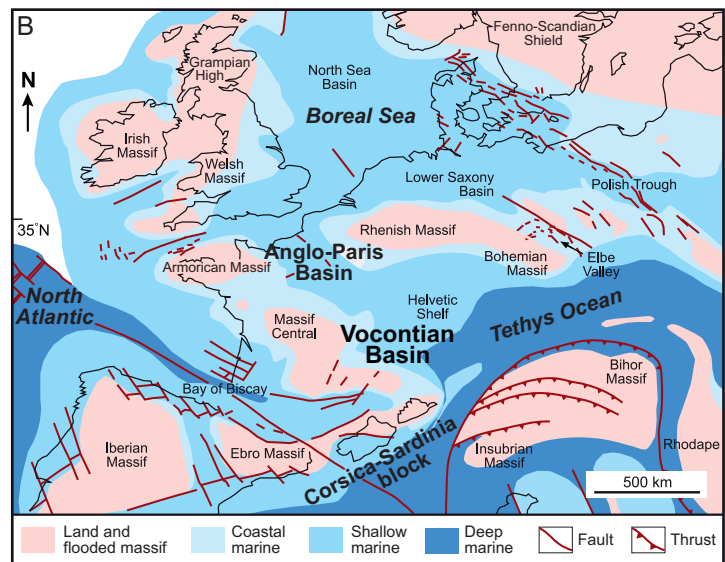
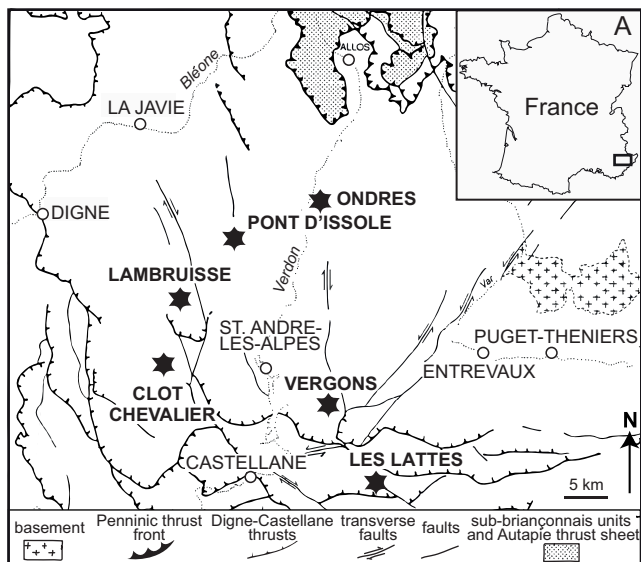
Z. erectus (Deflandre in Deflandre & Fert, 1954) Reinhardt, 1965

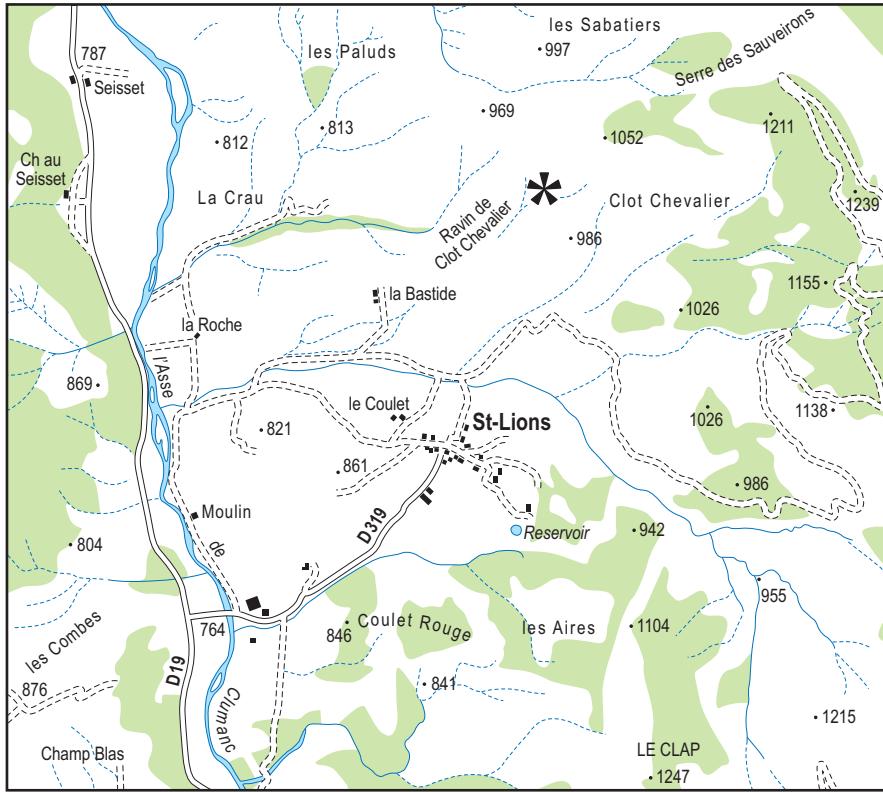
Z. howei Bown in Kennedy et al., 2000

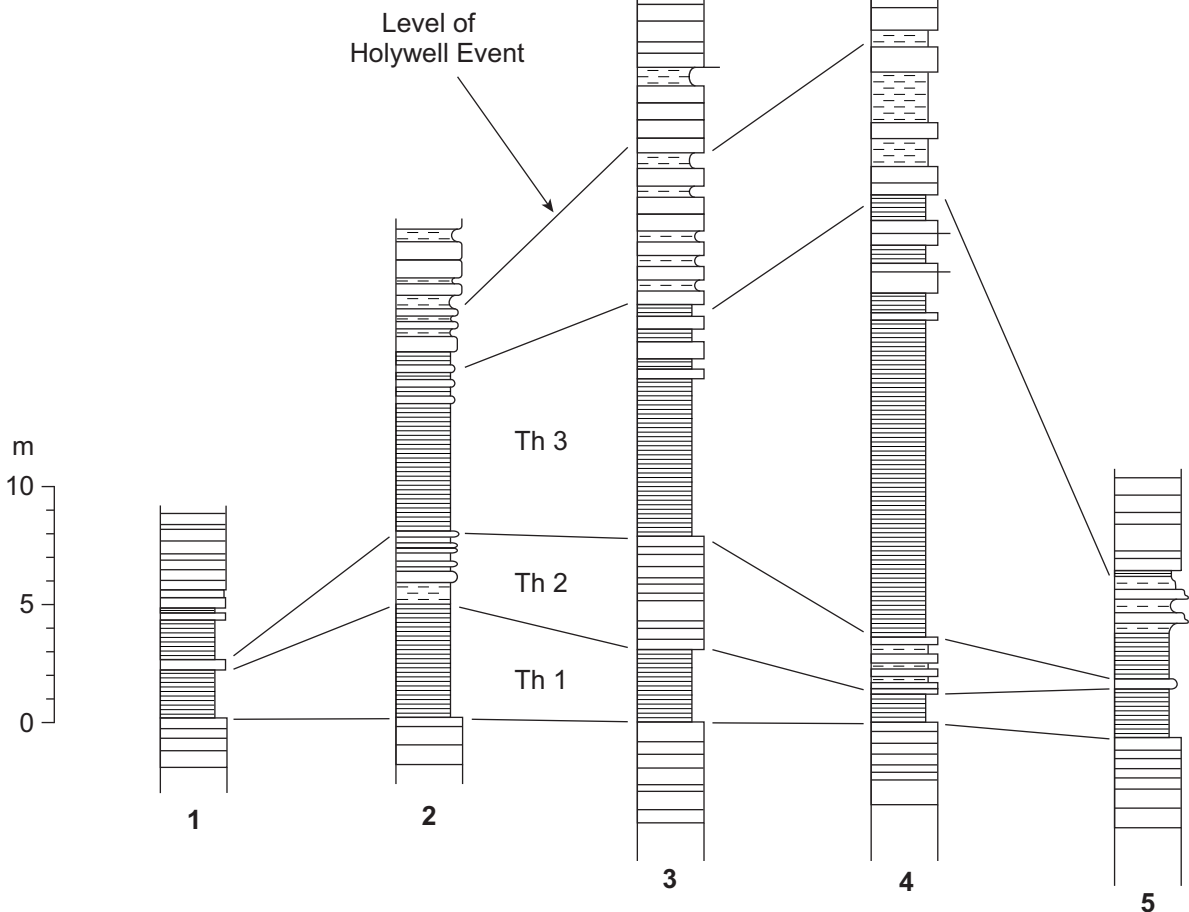
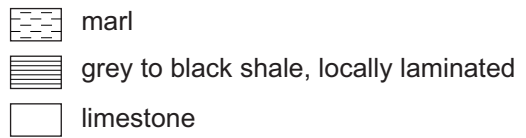
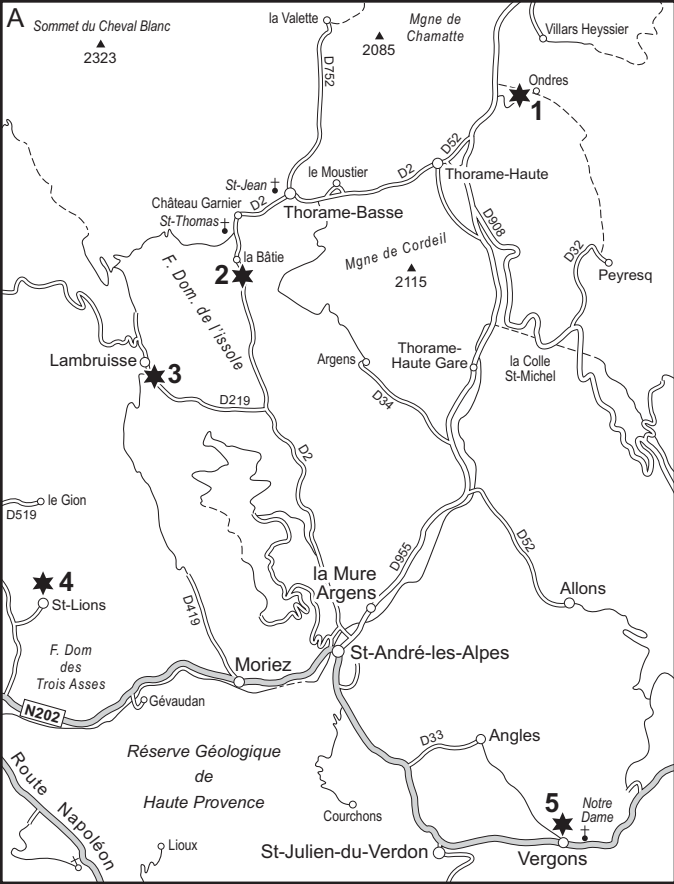
Z. noeliae Rod, Hay & Barnard, 1971

Z. scutula (Bergen, 1994) Rutledge & Bown, 1996

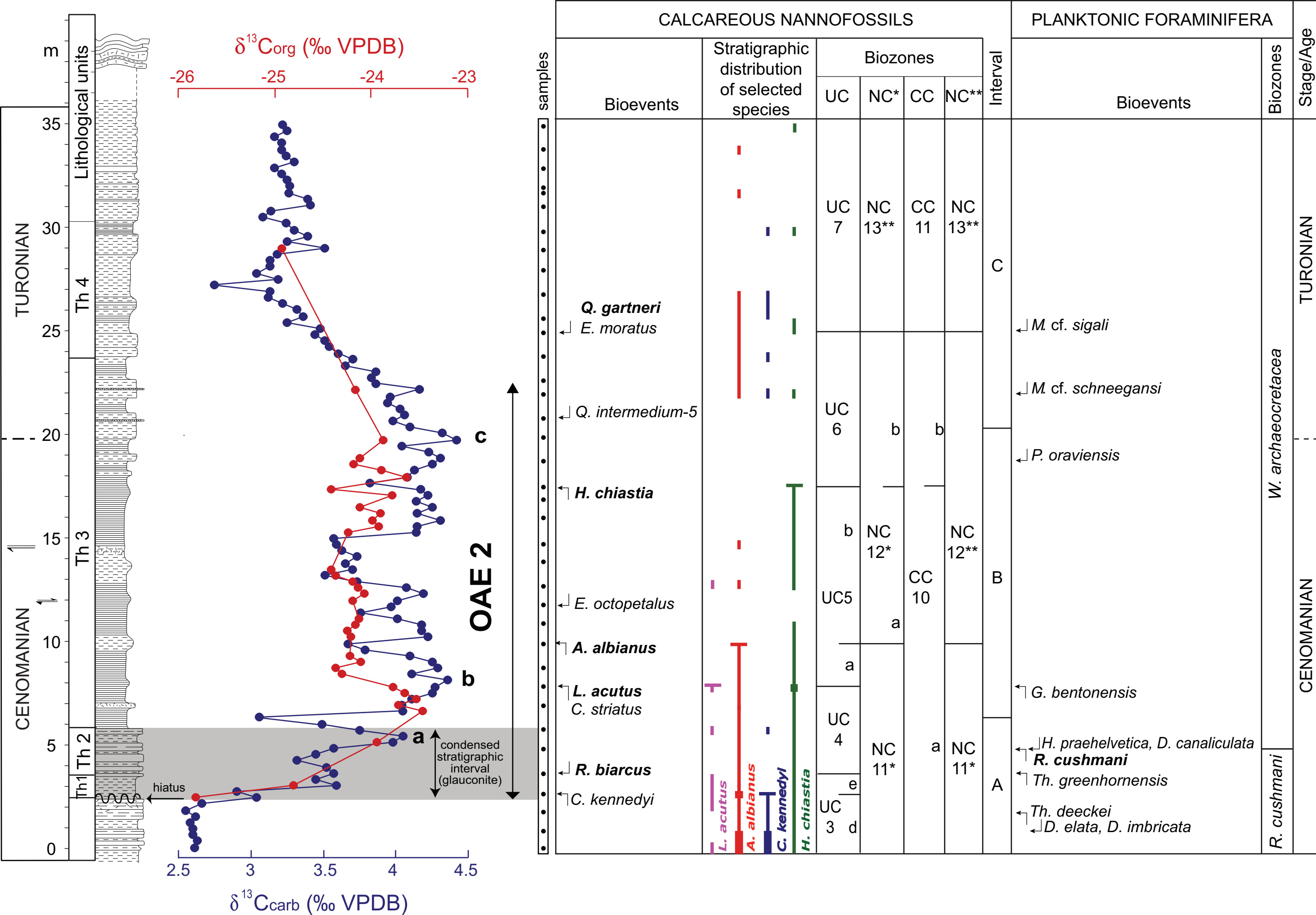
Z. trivectis Bergen, 1994

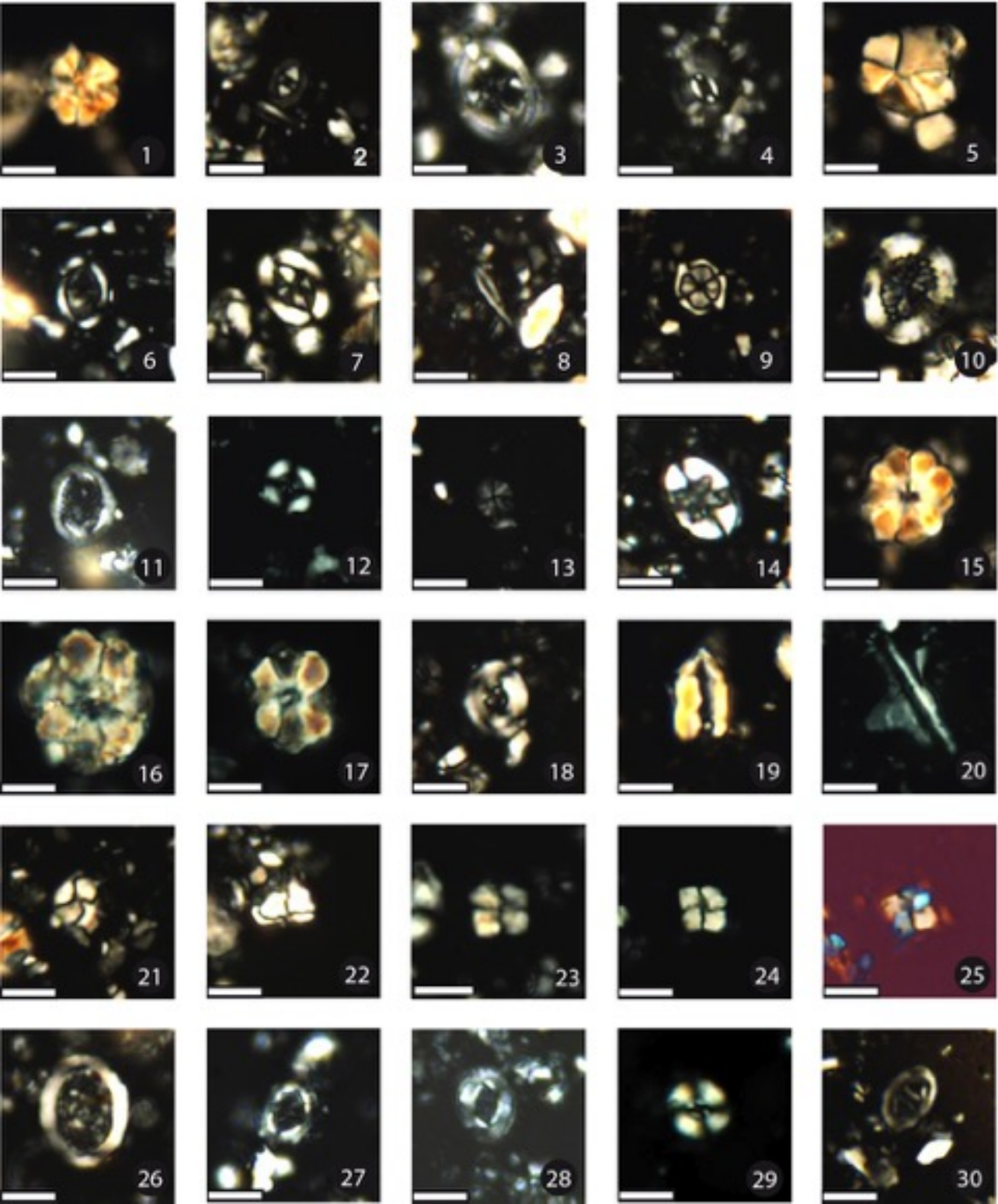


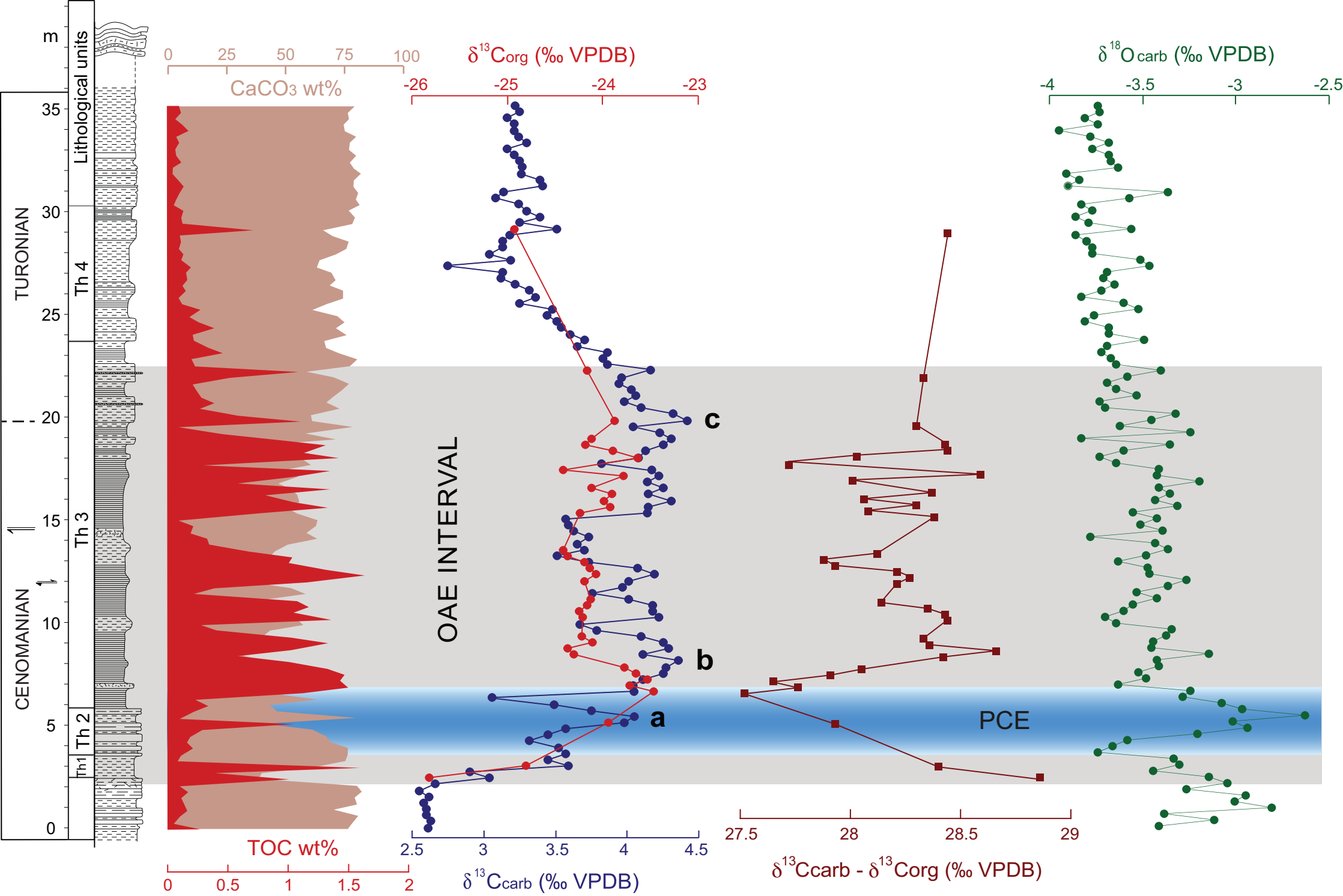


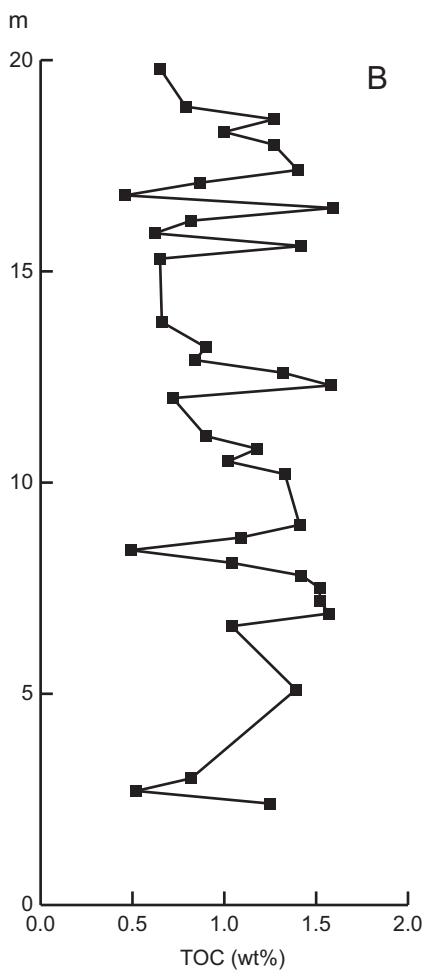
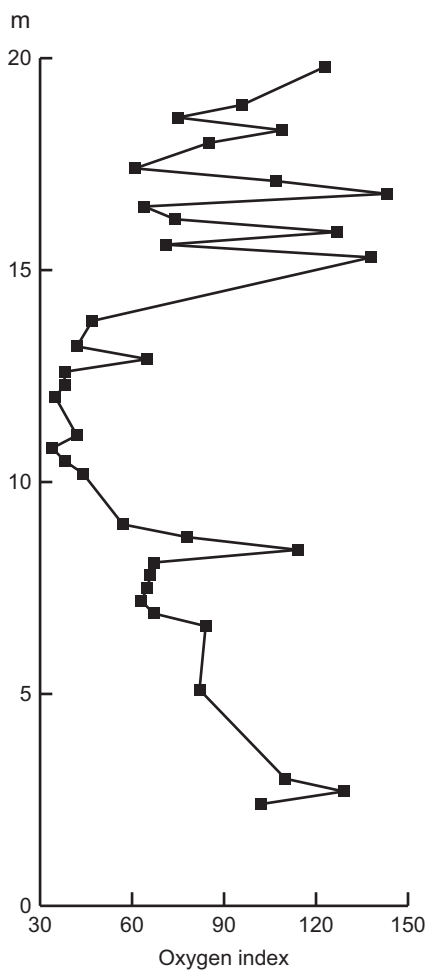
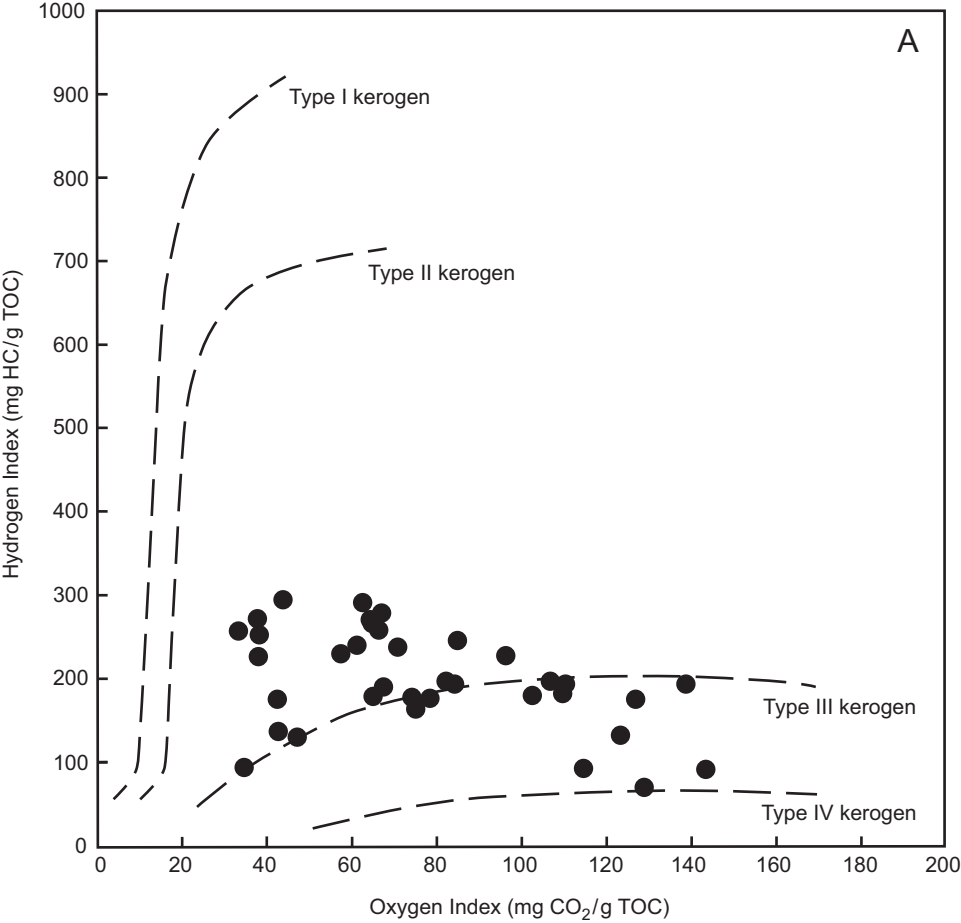


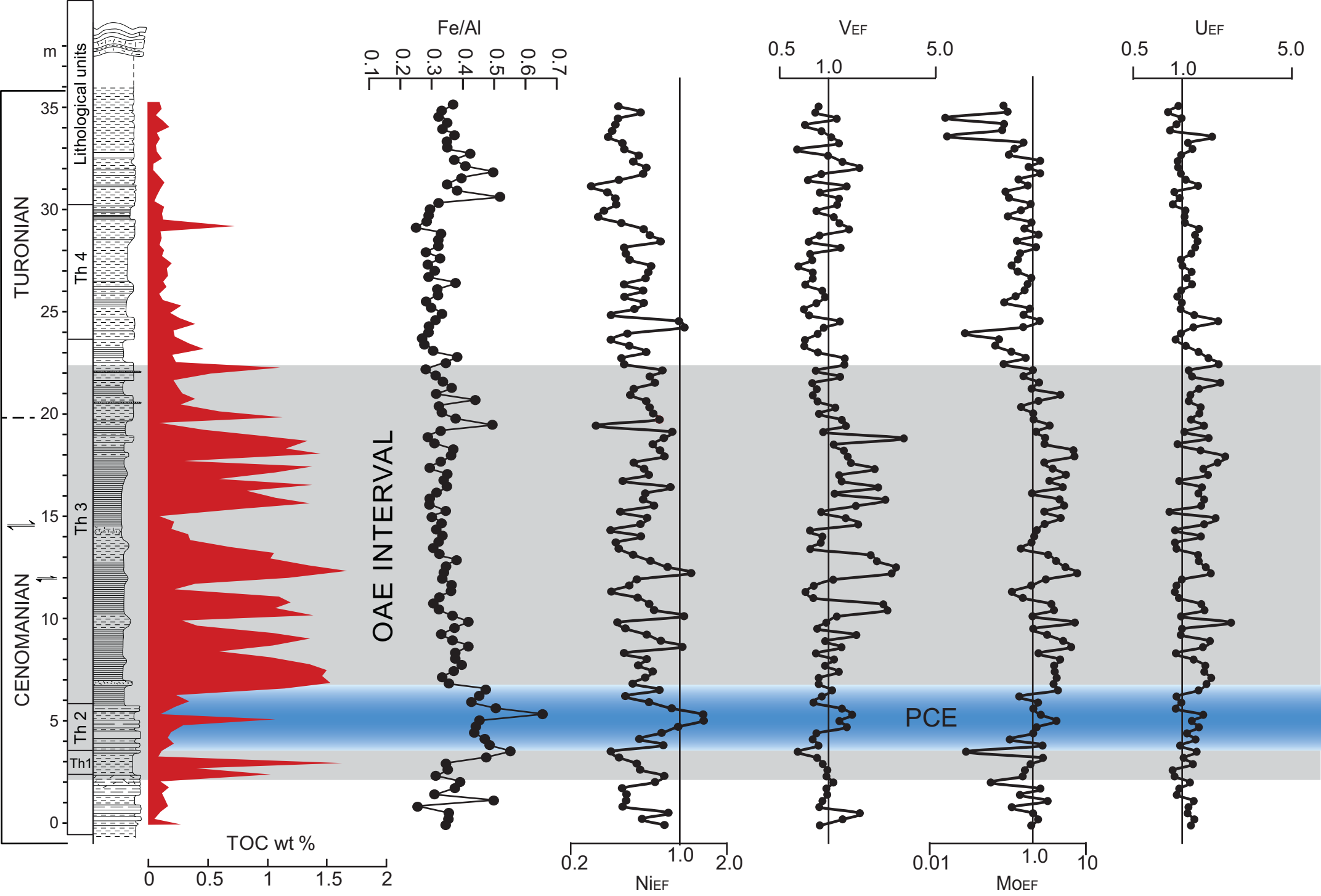


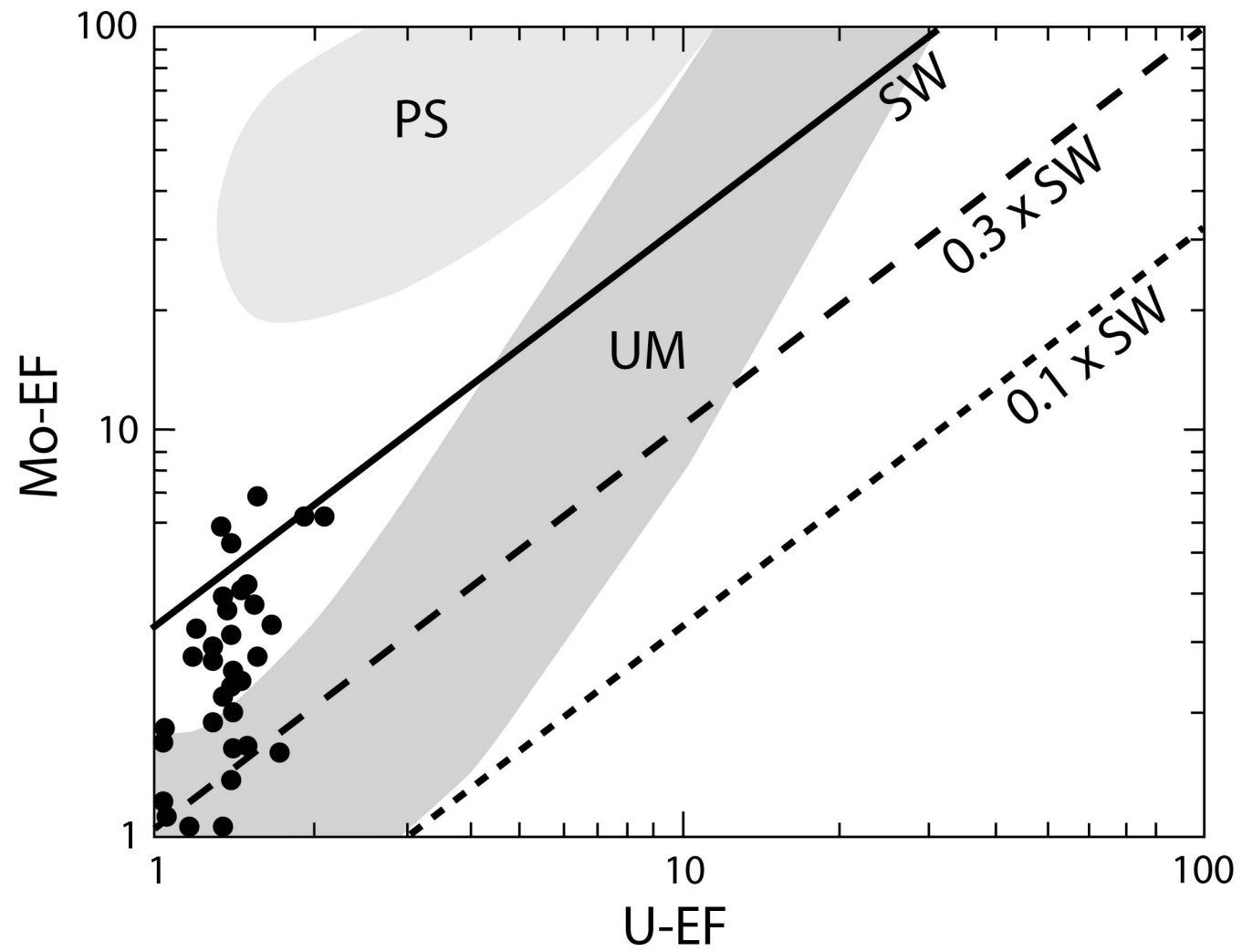


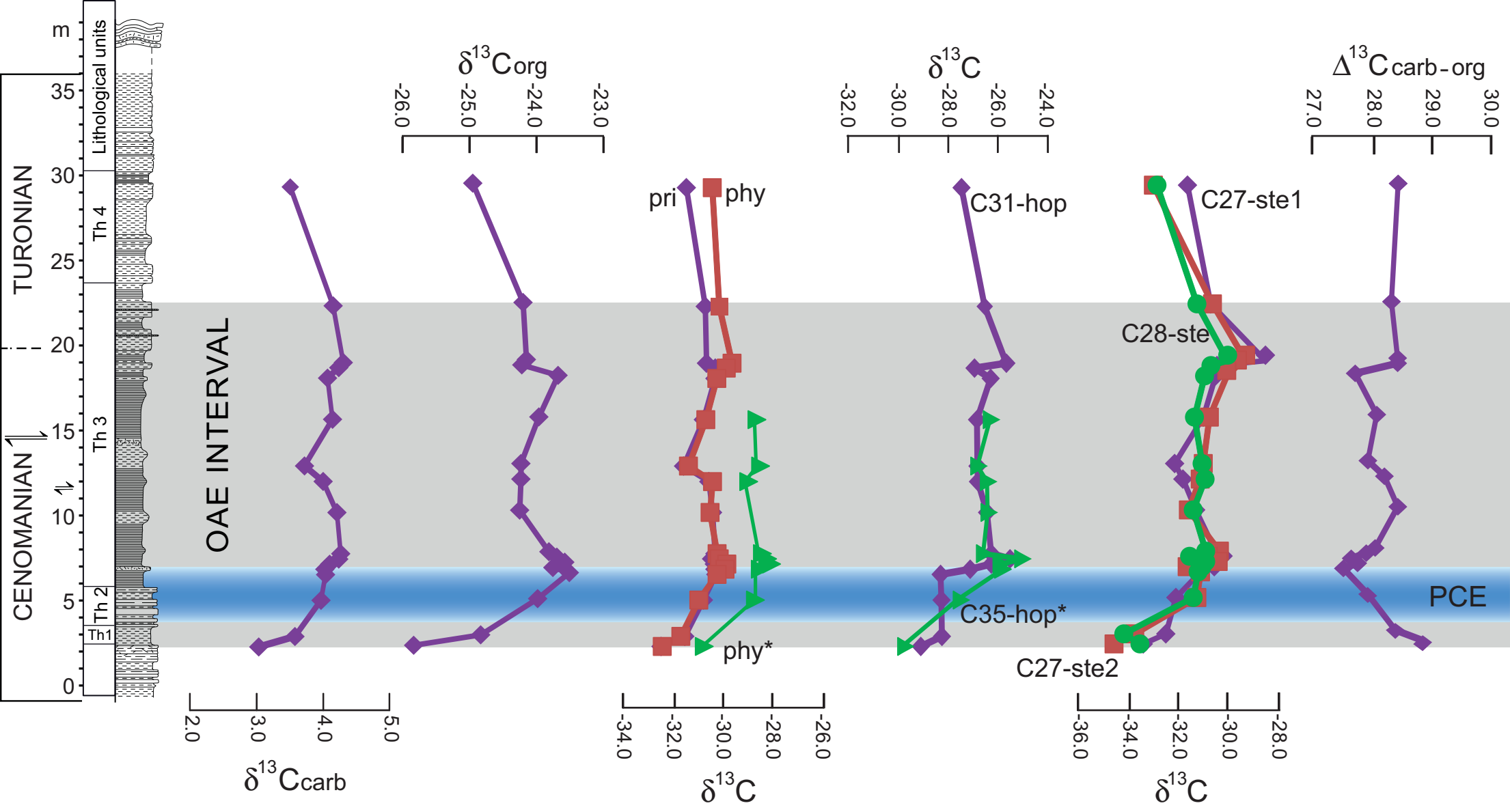


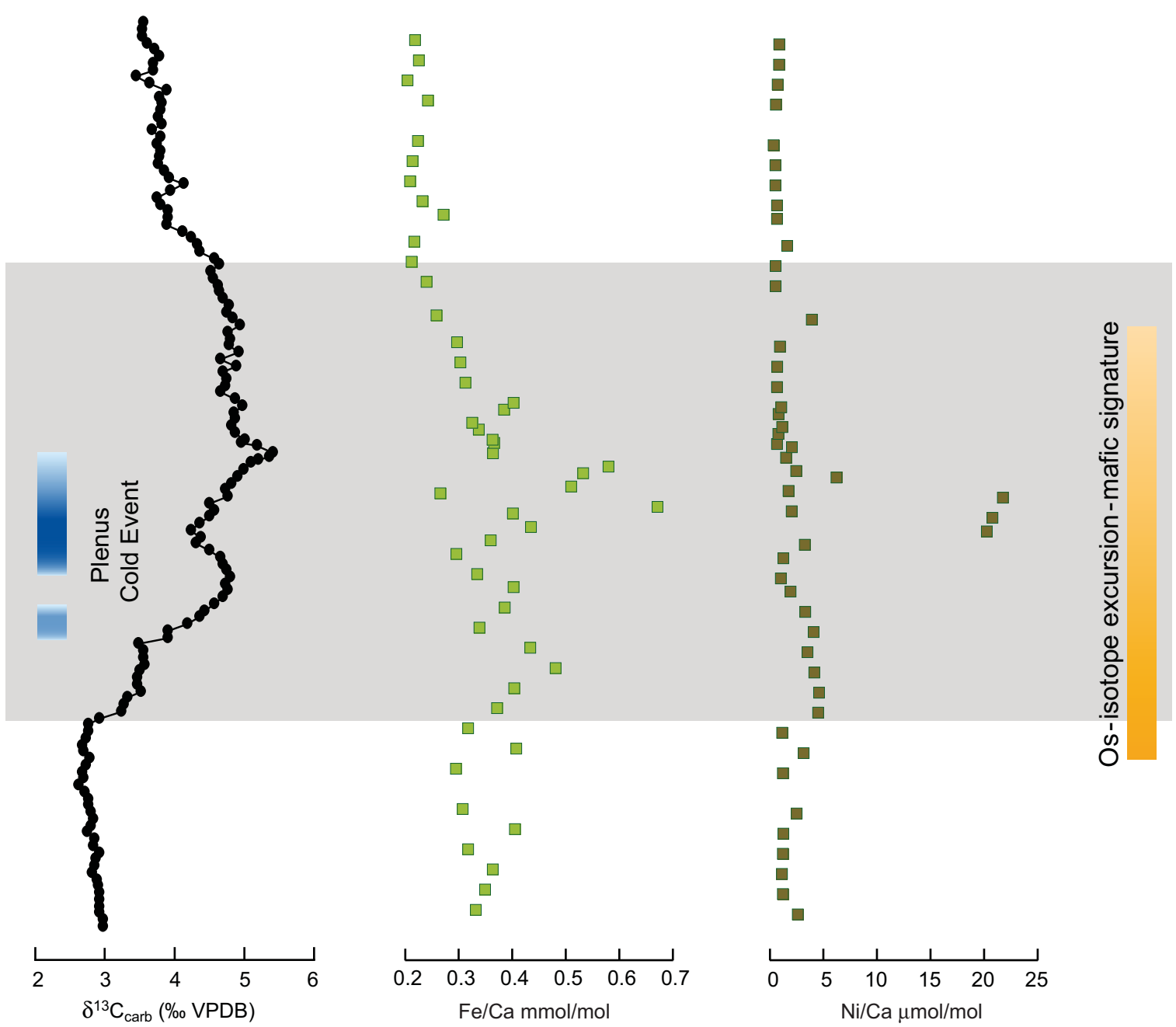
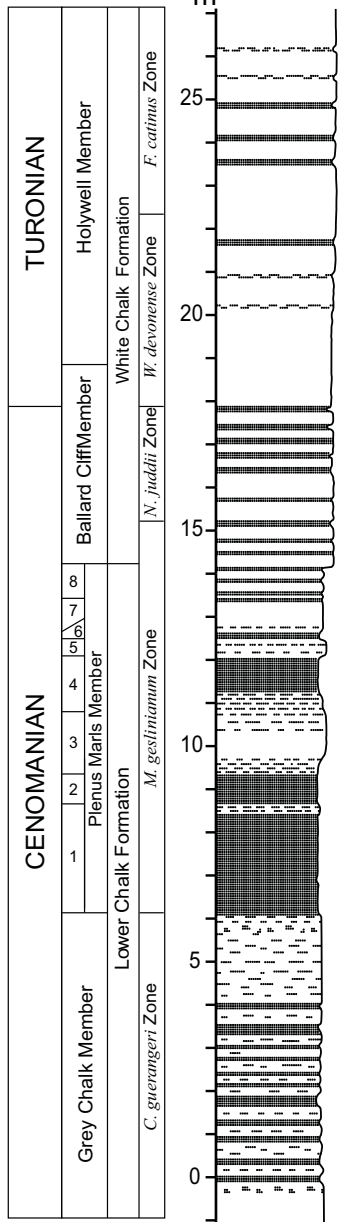












grey marls (clay-rich chalks)

white chalks with clay seams

white chalks

Bioevents	Sample	Depth (m)
LO <i>Dicarinella elata</i> ★	SLT 90	0.9
LO <i>Dicarinella imbricata</i> ★	SLT 90	0.9
HO <i>Thalmaninella deecke</i> ★	SLT 180	1.8
HO <i>Corolithion kennedyi</i> ❖	SLT 270	2.7
HO <i>Thalmaninella greenhornensis</i> ★	SLT 360	3.6
LO <i>Rotelapillus biarcus</i> ❖	SLT 360	3.6
HO <i>Rotalipora cushmani</i> ★	SLT 480	4.8
LO <i>Helvetoglobotruncana praehelvetica</i> ★	SLT 480	4.8
LO <i>Dicarinella canaliculata</i> ★	SLT 480	4.8
HO <i>Globigerinelloides bentonensis</i> ★	SLT 780	7.8
HO <i>Cretarhabdus striatus</i> ❖	SLT 780	7.8
HO <i>Lithraphidites acutus</i> ❖	SLT 780	7.8
HO <i>Axopodorhabdus albianus</i> ❖	SLT 990	9.9
LO <i>Eprolithus octopetalus</i> ❖	SLT 1170	11.7
HO <i>Helenea chiasia</i> ❖	SLT 1740	17.4
LO <i>Praeglobotruncana oraviensis</i> ★	SLT 1860	18.6
LO <i>Quadrum intermedium</i> 5 ❖	SLT 2070	20.7
LO <i>Marginotruncana cf. schneegansi</i> ★	SLT 2190	21.9
LO <i>Quadrum gartneri</i> ❖	SLT 2490	24.9
LO <i>Eprolithus moratus</i> ❖	SLT 2490	24.9
LO <i>Marginotruncana cf. sigali</i> ★	SLT 2490	24.9

LO = lowest occurrence

HO = highest occurrence

calcareous nannofossil bioevents ❖

planktonic foraminiferal bioevents ★

TABLE 2

	Carbonate	TOC	C31 hopane	Phytane	Pristane	C ₂₇ 20R Diasterene	C ₂₇ 20S Diasterene	C ₂₈ Diasterene	C ₃₅ hopane ^a	Phytane ^a
Carbonate	1.00	0.70	0.57	0.70	0.85	0.63	0.79	0.66	0.77	0.81
TOC		1.00	0.32	0.54	0.79	0.40	0.61	0.55	0.82	0.91
C31 hopane			1.00	0.51	0.36	0.56	0.56	0.45	0.82	0.68
Phytane				1.00	0.76	0.79	0.63	0.59	0.82	0.71
Pristane					1.00	0.51	0.62	0.57	0.72	0.71
C ₂₇ 20R Diasterene						1.00	0.67	0.57	0.72	0.69
C ₂₇ 20S Diasterene							1.00	0.87	0.68	0.85
C ₂₈ Diasterene								1.00	0.64	0.79
C ₃₅ hopane ^a									1.00	0.81
Phytane										1.00

^a in a sulfur-bound form